

# Power flow control in a substation of a wind- and solar farm

BSc. Graduation Thesis

Group 09.01

F.G.N. Rimon, 4652827

M. Mastouri, 4599470



# Power flow control in a substation of a wind- and solar farm

BSc. Graduation Thesis

by

Group 09.01

F.G.N. Rimon, 4652827  
M. Mastouri, 4599470

to obtain the degree of Bachelor of Science  
at the Delft University of Technology,  
to be defended publicly on X.

Student number: 4652827 4599470  
Project duration: April 2020– July 2020  
Thesis committee: Prof. dr. ir. J. Rueda Torres, TU Delft, supervisor

*This thesis is confidential and cannot be made public until X 2020*



# Abstract

Renewable energy generation is nowadays increasing around the world, especially wind- and solar power generation. However, increasing wind and solar power integration into the grid has a significant effect on the power system. The variability and uncertainty of these energy sources proposes new challenges for companies involved in grid management. In order to face these challenges, advanced control schemes and optimization algorithms has to be implemented in order to ensure stability and efficiency of the power flow. But these algorithms can only be implemented if the power flow in the system is modeled accurately. This thesis explains how the power flow in a substation of a wind- and solar farm in Zeewolde, the Netherlands, is modeled in order to guarantee efficiency and stability.

# Preface

The scope of this thesis is to provide an accurate model of the power flow in a substation with renewable energy sources, the Zeewolde wind-and solar park. The thesis is part of a project given by ABB. ABB aims to use this model as a complementary solution to satisfy TSO requirements at the point of common coupling with minimal losses in power and maximum stability. We would like to thank our supervisor dr. ir. José Rueda Torres for his exceptional guidance throughout the project. In cooperation with José, we were able to iteratively formulate requirements that would satisfy a realistic representation of the substation. Especially, dr. ir. José made an effort in providing the best quality of guidance under the COVID-19 circumstances. Furthermore, our gratitude is expressed for Dennis Groenenberg and Jan who constantly provided us with the information of the Zeewolde park needed for fulfillment of the scope of the project. Lastly, the complete project would not have been possible without the help of our colleagues, Alexandru Neagu, Dennis Groenenberg, Jin Han Bai and Laurens Beijnen. Because of you, the motivation stayed high while being in an enjoyable online atmosphere.

*Group 09.01*

*FG.N. Rimon, 4652827  
M. Mastouri, 4599470*

*Delft, May 2020*

# Contents

1	Introduction	1
1.1	Project objective . . . . .	1
1.2	Test models and state-of-art . . . . .	2
1.3	Thesis outline . . . . .	4
2	Programme of Requirements	5
2.1	Functional requirements . . . . .	5
2.2	Model requirements . . . . .	6
3	Model of the system configuration	8
3.1	Component modeling. . . . .	8
3.1.1	Cable modeling . . . . .	8
3.1.2	Transformer modeling . . . . .	10
3.2	Modeling the WTG farm . . . . .	10
3.2.1	Design of WTG on string level . . . . .	10
3.2.2	Design of the WTG capability curve . . . . .	10
3.3	Design of the solar farm. . . . .	11
3.3.1	Determination of solar farm parameters. . . . .	11
3.3.2	Solar farm overview . . . . .	13
3.4	Method to determine model accuracy . . . . .	13
3.4.1	Comparison to other Power Flow solving methods. . . . .	15
4	Test models for operating conditions	16
4.1	Hypotheses on results. . . . .	17
4.1.1	Active and reactive power losses . . . . .	17
4.1.2	Reactive injection losses . . . . .	18
4.1.3	Reactive power demand . . . . .	18
4.1.4	Expected system behaviour . . . . .	19
4.2	Wind farm procedure . . . . .	19
4.3	Solar farm procedure . . . . .	20
4.4	Hybrid farm procedure . . . . .	20
5	Results	21
5.1	Determination of model accuracy. . . . .	21
5.1.1	Comparison to other Power Flow solving methods. . . . .	22
5.2	Test Models for operating conditions . . . . .	22
5.2.1	Wind farm . . . . .	23
5.2.2	Shunt reactor on wind farm . . . . .	26
5.2.3	Solar farm . . . . .	27
5.2.4	Hybrid farm . . . . .	28
5.2.5	String level. . . . .	29
5.3	Prototype . . . . .	29
6	Conclusion	31
6.1	Conclusion . . . . .	31
6.2	Recommendations . . . . .	31
	Bibliography	32
A	Appendix	34
A.1	Additional overviews . . . . .	34
A.1.1	Group interaction . . . . .	40

A.2	Cable modeling . . . . .	41
A.2.1	Cable configurations . . . . .	41
A.2.2	Branch calculations . . . . .	43
A.2.3	Branch connections to bus. . . . .	43
A.3	Results . . . . .	43
A.3.1	Wind farm Plots . . . . .	43
A.3.2	Solar farm Plots . . . . .	46
A.3.3	Hybrid farm Plots . . . . .	49
A.4	MatLab codes . . . . .	52
A.4.1	Newton Raphson method . . . . .	52

# 1

## Introduction

In the past decade, the renewable energy market has increased significantly [26]. Equivalently, the current methods for energy provision such as coal, are becoming less popular. Ongoing research has the aim to make the transition to renewable energy as safe (f.e., no overloading) and efficient (f.e., no transmission losses) as possible [3].

### 1.1. Project objective

Ideally, once the substation is connected to the grid, the substation provides its full capacity at all times. However due to fluctuations in wind- and solar profiles, the Transmission System Operator (TSO) requirements cannot always be satisfied at the Point of Common Coupling (PCC) [14]. There is also loss in several of the components which form the subsystem such as power loss in the transmission lines, bus bars, transformers and even in the Wind Turbine Generators (WTGs) and PV panels. Since these losses will effect the power generated and the power delivered at the Point of Common Coupling, they have to be taken into account in order to implement an accurate model for the system.

In the stator rotational energy of the blades of the wind turbines is converted into electrical energy. Since the conversion is made with magnets, AC current production occurs. This gives rise to different AC voltages on the nodes of the power system of the wind modules. These voltages can be lagging or leading to the current in the power system, which gives rise to either absorbing or generating reactive power by the wind turbines. However, at the nominal value of 1 p.u, the voltages will not be lagging or leading, but in phase with the current, which will result in no reactive power. One of the requirements of the Transmission System Operator is to control the reactive power and assure that, when needed, the reactive power at the Point of Common Coupling is brought to zero.

The power in the PV module is generated in DC conditions. Hence, the solar modules do not generate any reactive power. Since the transmission grid operates in AC conditions, the DC power has firstly to be converted to AC in order to be fed back into the grid. For this conversion process, DC/AC inverters are used. These inverters will either generate or absorb reactive power [24]. This reactive power has to be taken into account in order to design an accurate as possible solar farm.

In addition, advanced control schemes are designed to find the optimal setpoints in the substation that satisfy TSO requirements. The setpoints indicate the power flow through each generation string. The optimisation is based on the system's configuration and non-idealities, but also on the grid code requirements <sup>1</sup>. This mathematical scheme cannot determine the feasibility of the given setpoint in reality. It needs information of the substation's power flows. Through communication between the modeling and optimization entity, the scheme can make its search space smaller and find a global optimum.

The project aims to use the case study, shown in Fig. 1.1, to design an accurate model of the power flows

---

<sup>1</sup>"Grid codes specify the electrical performance that generation assets must comply with in order to obtain the required approval for its connection to a grid." [8]

that shows the effects of fluctuating wind/solar profiles and components' non-idealities. When the optimization algorithm sends setpoints to the model, the model returns the actual feasibility by providing the power flows in each of the branches in the system configuration. Dependent of the development status of a project, this model can indicate if the system configuration is to be improved/changed. Additionally, it provides the feasibility for future expansion of the substation without violating any physical constraints. Steadily, increasing the RES generation for the growing energy demand worldwide.

For the scope of this project, a realistic model of the system behaviour shall be designed and tested. The models for the PV- and WTG farm of the case study are combined and tested under critical conditions, such as low wind speed, low solar irradiance, or both for high reactive power requests from the TSO. The problem formulates: "When is the system able to satisfy high load demands at the PCC under critical, i.e. too low or too high, generation of power from the renewable energy systems?"

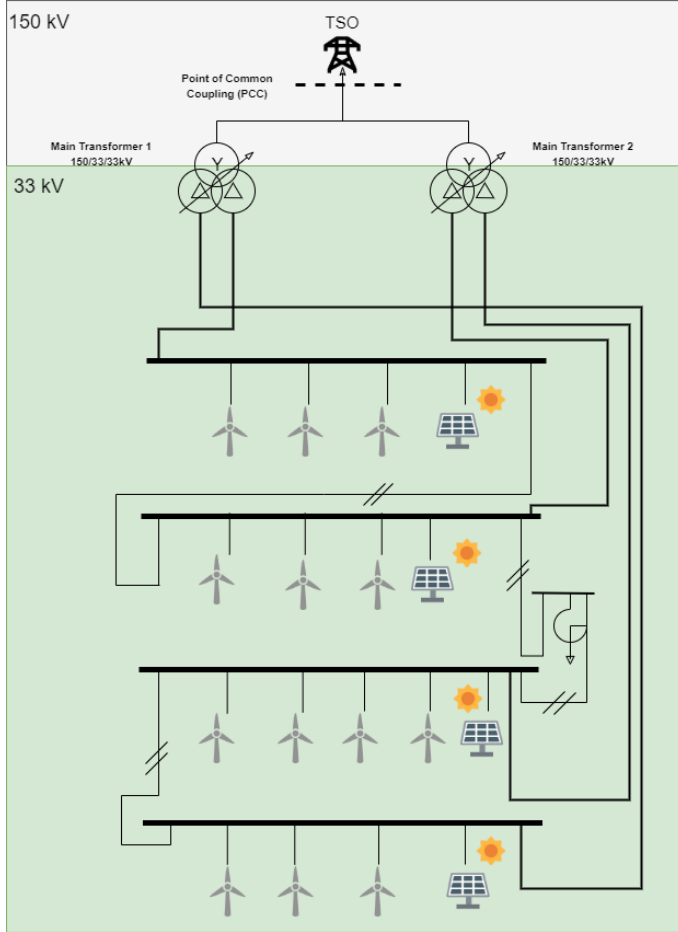


Figure 1.1: Simplified schematic of case system

## 1.2. Test models and state-of-art

In order to perform several power system analysis, information about the power system is needed, which consists of the system topology and nodal power injections. The nodal power injections consist of active- and reactive power, which are either measured or determined. In Fig. 1.2 the input and output data of an iterative power flow calculation is shown.

Furthermore, in the iterative power flow calculation block certain equations are applied. The generic equation, as shown in Eq. 1.1, will be used in order to generate the voltage magnitude p.u and angle of all nodes iteratively. However, there is one bus, frequently allocated to the bus at the PCC, for which the voltage magnitude p.u and angle are known. This bus is called the slack bus. In this bus the active and reactive power

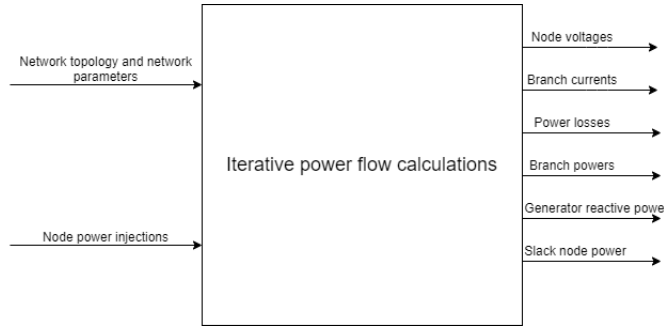


Figure 1.2: Block diagram with the input and output data in order to perform power flow calculations.

injections are determined with the known voltage magnitude p.u and angle in order to check whether certain requirements at the PCC are fulfilled. In the remaining nodes the voltage magnitude p.u and angles of the busses will be determined with the known values of the active and reactive power injections. These busses are called PQ-busses and are used since they give rise to a set of finite equations, which will result in a finite number of solutions for the magnitudes and angles. For the PQ-busses, there are in principle two equations generated, one for the active power and one for the reactive power, as shown in Eq. 1.2 and 1.3. Since the unknown variables in all PQ-busses are the voltage magnitudes p.u and angles, a state variable matrix  $\mathbf{x}$  can be constructed, as shown in Eq. 1.4, from which all the PQ-busses can be solved iteratively by solving Eq. 1.5.

$$I_{[Nx1]} = Y_{bus_{[NxN]}} \cdot U_{[Nx1]} \quad (1.1)$$

$$P_i = f_p(U_1, U_2, \dots, U_N, \delta_1, \delta_2, \dots, \delta_N) \quad (1.2)$$

$$Q_i = f_q(U_1, U_2, \dots, U_N, \delta_1, \delta_2, \dots, \delta_N) \quad (1.3)$$

$$\mathbf{x} = [\delta U]^T \quad (1.4)$$

$$f(\mathbf{x}) = 0 \quad (1.5)$$

Different algorithms have been designed to solve  $\mathbf{x}$  in Eq. 1.5 in an iterative manner. Reason for more algorithms are its solving (or convergence) time and accuracy for specific networks. These modern algorithms still make use of the two conventional approximation methods, Gauss-Seidel method [11] and Newton Raphson method [23]. Gauss-Seidel is a simpler technique requiring less computation per iteration. The computation time is sensitive to the system parameters. Therefore, the majority bases the algorithm on Newton-Raphson, since the system converges in less iterations, which gives smaller computation time, more accuracy and makes it less sensitive to other system parameters. This makes it suitable for a complex system, as shown in Fig. 1.1. A more precise schematic is visible in App. A.1.

A fluctuation in wind/solar profile, causes a fluctuation in the power generated. Current methodology takes this fluctuation in wind/solar profiles by designing algorithms that describe a probabilistic behaviour of wind speed and solar irradiance [4] [6] [2]. This probabilistic behaviour is to test the system under the most common operating situations, i.e. common wind/solar profiles, since little variation from the rated wind speed is included to the model. Additionally, the probabilistic model offers the possibility to create both random load demands and generation capabilities in the system at random dispatches. Therefore occasionally violating physical constraints of the system. This offers a test model for alert operating conditions<sup>2</sup>. Hence, the probabilistic model offers a suitable test model under different operating conditions. Compared to use of historical data, which can vary throughout time periods (per season or year), this test model runs more situations.

<sup>2</sup>alert operating conditions in which physical constraints are violated or there is a high vulnerability to disturbances

To model daily wind profiles, research makes use of, a Weibull distribution, historical data or a versatile distribution that combines Beta, Cauchy and Gaussian to model a daily wind profile [27] [13]. However the majority makes use of Weibull PDF, since it was determined that the distribution resembles real life situations the most [25] [18] [13].

For solar irradiance, each research makes use of an own model. These models can be divided into: Design based on historical data and chosen PDF [29], Beta distribution [9] [13] or Weibull distribution [9], design based on spatio-temporal stochastic model with each spatio(or season such as sunny, cloudy,etc.) having own stochastic parameters[21].

Out of these models, the probability for output power is determined. This offers a solution in case of insufficient or inaccurate wind-and profile data. Other research, suggest a  $\pi$ - model of the individual WTGs and PV panels to determine the output active- and reactive power. It makes use of properties of the system. This provides an accurate solution if all data is known, i.e. datasheet of the WTG as well as the profile data [20] [10] [24]. For the probabilistic model of the RES, the reactive power output is unknown in case of insufficient data about the system itself.

Due to its maturity and proven performance as open source tool, Matpower was selected for the design of a model in steady state and AC conditions. MATPOWER is a MATLAB package aiming to solve steady-state power simulations [28]. For this model the basic Newton-Raphson method is used. More sophisticated methods would be possible if the system was a radial network, where each load has its own generator. The system configuration in Fig. 1.1 analyses a network system, which has multiple generating sources for a single load. Also, the sophisticated methods, are focused on reducing computation time, which is not part of the scope for this project.

The challenge for this project is to have an accurate model of the power flow for a substation that combines both wind-and solar generation under normal and extreme weather conditions. The state of art does not seem to analyse such a case study. Research does address the effects of such a substation on the transmission grid, but not on the substation. In addition, there shall be looked at the loss effects of the 3-winding transformers. These will be approximated with an equivalent 2-winding transformer model. The sub group responsible for optimisation shall find the optimal tap position and send it to the modeling subgroup. This interaction is visible in Fig. 2.1.

Due to insufficient data of both wind profile and WTG's components for the specific case study, using only one model will yield inaccurate results of the power flow. To model such WTGs under fluctuating wind profile conditions, the best model is achieved by combining both methods. The different operating conditions is tested with the probabilistic behaviour, while the PQ/RX model determines the exact output of wind modules after internal losses. Therefore, a correct estimate of the active, reactive power generation and voltage profile is formulated for each dispatch profile.

Next, the same can be done for the PV modules. The models for reactive power capability and probabilistic solar irradiance are combined. In reality, most of the time, both PV- and WTG farm will be active. All generating strings, Fig. 1.1, influence the system simultaneously in normal-and critical operating conditions. With the farm being fully active, voltage profiles can deviate a lot from the ideal 1 p.u., leading to violation of technical constraints.

### 1.3. Thesis outline

To formulate a correct answer for the project objective, the thesis will delve into the necessary requirements to determine what it means to have an accurate power flow model. Once requirements are determined (Chap. 2), a procedure will be followed on the model of the system (Chap. 3) and subsequently, the behaviour of the system model is determined under different operating conditions (Chap. 4). Then, results are assembled and analysed (Chap.5). Out of the results, a conclusion is made (Chap. 6) Additionally, recommendations are made for future research related to this project subject and a discussion about the results can be formulated. This discussion offers room for improvement and recommendations for future researchers modeling power flows for similar case studies.

# 2

## Programme of Requirements

### 2.1. Functional requirements

As mentioned in Chap. 1, to formulate a correct research, the problem shall be divided in smaller subproblems. The model should be able to:

1. Update the components' parameters in the system topology after every setpoint iteration.
2. Indicate when constraint limits of voltage and/or current are violated in each branch or bus of the substation.
3. Indicate losses and injections of each branch and bus of the system for given setpoints.
4. Take influences into account for power generation due to fluctuating wind- and solar profiles.

To determine how the model will indicate if requirements are satisfied, one needs a correct definition of setpoints received from the optimization scheme. The interaction of the subgroups is specified in Fig. 2.1. The interaction between the three components of the optimisation unit is found in App. A.7. For the case study, the setpoints will be given in the form a dispatch vector, which indicates the required reactive power from the generating strings, 13 WTG strings and 4 PV strings, shown in App. A.1. Additionally, the connection status for the reactor is required. Usually the reactor is disconnected, but if the optimization scheme requires this in order to satisfy reactive power at the PCC, the reactor will absorb reactive power (-12 MVar).

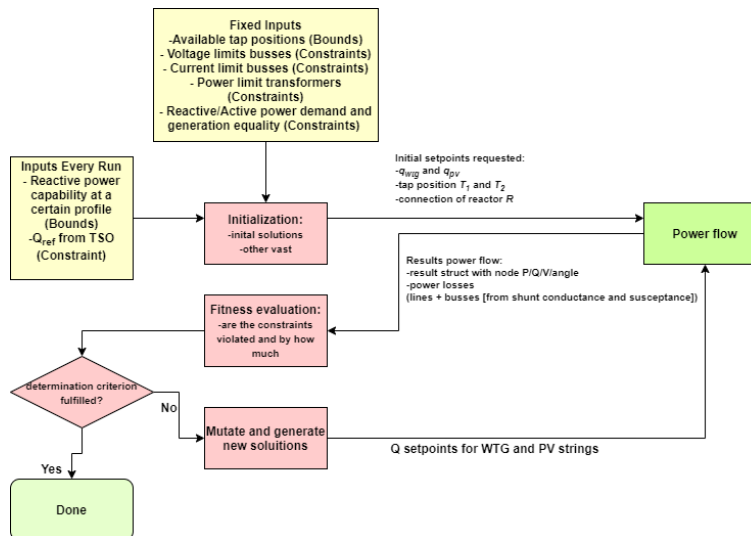


Figure 2.1: Interaction between optimization and modeling of the power flows

## 2.2. Model requirements

The sub problems are formulated in Mandatory requirements, Trade-off requirements and optional requirements. Mandatory requirements are:

1. To take the influence of each component in the system into account:
  - (a) Formulate a system topology which connects each node of App. A.1. Hereby, all information of the system is implemented. This includes the PCC, wind- and solar PV strings, transformer- and cable data.
  - (b) The design of the solar farm. This overview consists of the interconnection of the solar modules, the cable types and the type of DC/AC converters used.
  - (c) To determine the reliability of the implemented case system, power flows are compared to own hand calculations that apply the theoretic approach [23].
  - (d) After completion of the first two requirements, the system topology is formulated on string level. Hereby, the system topology is updated with the subdivision of individual WTGs at each string. Each WTG has its own rated power output, cable and inverter type connection. More will be explained in Subsec. 3.2.1.
2. To determine the system behaviour for every possible operating condition:
  - (a) An analysis of the system behaviour for different operating conditions. From this, the relation is determined between total losses, injections and voltage profiles for each combination of generation and demand. This includes extreme combinations for which the power demand will not only come close to generated power, but also exceed generation of the strings.
  - (b) An analysis on the behaviour of components that cause most voltage physical violations and losses.
3. For proper communication between the requests of the optimization controller and the model:
  - (a) The system topology has to be updated twice after each given setpoint. The first update is to change the active and reactive power generation according to the wind and solar dispatch. The second update is to change the reactive power of the generation strings.
  - (b) Before receiving setpoints from the optimization scheme, the available active and reactive power, with tap positions from each transformer is sent to the optimization scheme. With this information and system, the optimization scheme can determine the initial vector of string setpoints.

The satisfaction of mandatory requirements can be tested once the system converges on MatPower for a Newton Raphson power flow [28], after the system parameters are updated or sent to the optimization scheme.

Trade-off requirements are necessary in order to improve the research in a stepwise manner. This results in conclusions that can be used for future expansion of the case study used, since its behaviour is modelled for every possible conditions. Therefore, trade-off requirements are:

1. Include losses generated by changing the tap position of the equivalent model of the 3-winding transformers. This tap position is updated in the system topology according to the procedure in Fig. 2.1.
2. Include losses generated by the equivalent model of the 3-winding transformers' inner-and outer winding in the transmission lines.

Furthermore, there are also optional requirements, which are not needed to design, implement and test the model, but can be implemented in the future in order to add new insights to the research, namely:

1. Design the PQ and RX models used in state of the art research in order to model the PQ-capability curves of the wind turbines [20]. However, for this research the PQ-capability curves of the WTG's were available [19] and no data is supplied about the impedances of the rotor and stator of the WTG's. This resulted in considering the implementation of the PQ and RX models as an additional requirement. In a later phase, the PQ and RX models could be designed using data from other researches in order to give an as accurate as possible estimation of the PQ-capability curves. Eventually, these estimations can be used in order to give a comparison between two different modeling methods.

Additional requirements are needed for the proof of concept. Hereby, the design of a visualization model for the Single Line Diagram of the case study, with the power flow and losses indicated after every system update [19]. Note: For the prototype, it is not of importance which component, i.e. cable or transformer, generates the loss.

Concluding, once mandatory requirements are satisfied, the model will prove to be accurate for power control at the PCC, because it includes transmission losses and most importantly, the behaviour of the wind-and PV modules for rated power output. In addition, trade-off requirements will supplement the model by testing the system configuration under different situations determined by the probabilistic behaviour. Furthermore, optional requirements firstly add a new level of accuracy to the model, since additional losses in the farms are accounted for. Secondly, they could give new insights to research, since results of state of the art models are compared with the results of the models used in this research. Additionally, losses of previously ideally assumed components are included, providing actual power flow in the system topology.

# 3

## Model of the system configuration

For the design of the model, the data in [19] [16] was used. This offers the configuration with assigned bus numbers, cables', transformers' type and length shown in App. A.2. Here, the rightmost generation string of bus bar 7,12,16,23 are the PV strings. In App. A.1, the system configuration is shown with maximum voltages for bus bars and maximum current for branches. On the left, the base voltage is indicated for each section of the substation.

Since [19] offered insufficient data of capability curves of the WTG and PV-farm, certain assumptions were made. Firstly, it was decided to make the slack node the PCC, i.e. bus bar 1. The voltage magnitudes and angles of each bus were compared to the PCC node, with a magnitude of 1 p.u. and 0 degrees. To implement the constraints for the voltage profile, it was decided to determine this from the main transformer data. The transformer data indicates the maximum input/output voltage and current. These values are shown in Tab. 3.1. Although the cable type can handle more, the main transformers set the power flow limits for the system configuration.

### 3.1. Component modeling

#### 3.1.1. Cable modeling

Different branches in the system topology had different three-phase configurations. It was decided to model this configuration, using an equivalent  $\pi$  transmission line model. In Fig. 3.1, each branch will have a starting node, i.e. "Bus from", and ending node, i.e. "Bus to". The branch between these nodes has a series impedance,  $Z_s$ , consisting of a real and imaginary impedance. The injection charge of busses is modelled with a parallel charging susceptance,  $b_c$ . Some of the branches are transformers. To specify this in a systematic manner, each branch has a transformer with a tap ratio, i.e. N. For most branches this ratio is equal to 1. The phase shift,  $\theta$  between nodes is unknown and therefore considered to be its ideal value of 0.

To calculate the  $\pi$  model values for each branch of the system in App. A.2, the cable type and configuration were determined. The DC resistance value for a nominal temperature of 20 degrees Celsius was assumed. The configuration is specified with AxBxCxD mm<sup>2</sup> "material". **A** specifies the amount of cables per single phase. **B** specifies the amount of phases, i.e. in this system it is a three-phase system for each node. **C** specifies the amount of parallel cables in one single phase cable. The extra C stands for "cable", indicating where the single phase specification commences. **D** specifies the cross-section area of the cable in mm<sup>2</sup>. An example of the configuration is shown in Fig. 3.2. Diagrams of other configurations are found in App. A.2.1.

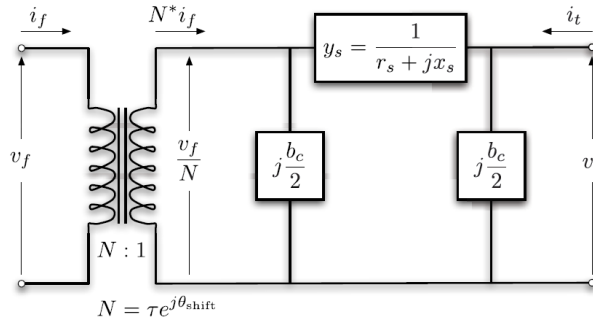
After specification of the cable configuration, the parameter values are calculated to per unit to have a more uniform definition of the differences in absolute values. Tab. 3.2 specifies the parameter values of the

Table 3.1: System constraints based on transformer data

	V <sub>max</sub> (kV)	I <sub>max</sub> (A)
primary side	33	735
secondary side	171.316	808.6

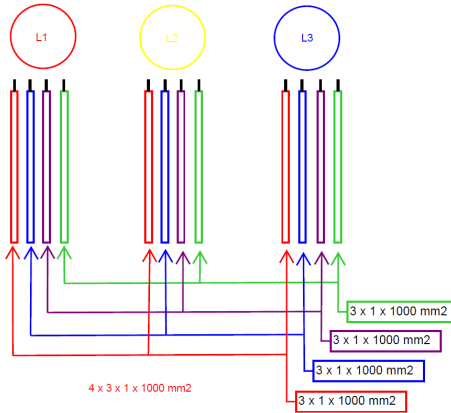
Table 3.2: Absolute impedance and capacitance values per km of cable types. Data acquired from [19].

Cable	Resistance (Ohm/km)	Reactance (Ohm/km)	Capacitance (e-6 F/km)	Apparent power rate (MVA)
3x1Cx2500mm <sup>2</sup> XLPE Al	0.0119	0.06788	0.3	400
1x800mm <sup>2</sup> AAC Conductor	0.0356	0.101	0.366	400
2-winding transformer	0	0	0.2025	240
3x1Cx1000mm <sup>2</sup> XLPE Al	0.0291	0.1666	0.38	46.2977
4x3x1Cx1000mm <sup>2</sup> XLPE Al	0.007275	0.0415	1.52	185.19
3x630mm <sup>2</sup> Cu	0.0283	0.163	0.35	36.86
3x630mm <sup>2</sup> Al	0.0469	0.177	0.32	36.86
3x400mm <sup>2</sup> Al	0.0778	0.19	0.26	28.29
3x240mm <sup>2</sup> Cu	0.125	0.196	0.22	20.86
3x150mm <sup>2</sup> Al	0.206	0.208	0.19	16.28

Figure 3.1: Equivalent  $\pi$  transmission line model for the branches of the system topology, Fig. taken from [28].

branches per km. Multiplying it with the distance of the specified branch, the absolute value is obtained. Eq. 3.2 describes the calculation of the base impedance. The base voltage is dependent of the region where the branch is, i.e. two regions. The first region is the secondary side of the transformer with a 150 kV output voltage. The second region is the primary side of the transformer with a 33 kV input voltage. For the sake of simplicity, a base power of 100 MVA is chosen for the entire transmission system. After the base impedance is calculated for the specified region using Eq. 3.2, Eq. 3.3 calculates the per unit values for each branch. Similarly, the susceptance is calculated. Additionally, the apparent power rates of the branches have to be determined in order to satisfy the power limits of the system. The rated apparent power is determined using Eq. 3.1.

$$S_{Rated} = \sqrt{3} \cdot I_{Rated} \cdot V_{Base} \quad (3.1)$$

Figure 3.2: Configuration of a branch with XLPE 4x3x1Cx1000mm<sup>2</sup> Al cable. Data from [19].

$$Z_{base} = \frac{V_{base}^2}{S_{base}} \quad (3.2)$$

$$Z_{perunit} = \frac{Z_{absolute}}{Z_{base}} \quad (3.3)$$

All branches are modelled, but there are specific branches that are considered to be disconnected unless stated otherwise by the optimization setpoints received. Firstly, **The shunt reactor** is assumed to be disconnected. Therefore, branch 12-28 and 17-28 are disconnected. Ideally, this is connected only in the case that the generating strings are unable to satisfy a specific amount of reactive power demand from the TSO. Additionally, if negative reactive power is needed in the system to prevent violations of constraints. The influence of the shunt reactor is analysed in Chap. 4.

**Branch 7-12 and 17-23** are disconnected. These branches are safety branches in case of faulty conditions, i.e. overcurrent or overvoltage at the bus bars. The current will in such case be higher than 2500 A, or higher voltage than 36 kV, shown in App. A.1.

### 3.1.2. Transformer modeling

In order to model the main 3-winding transformers shown in App. A.1, a 2-winding approximation is implemented as shown in Fig.3.3. Eq.3.2 is used in order to calculate the  $Z_{base}$ , in which the base voltage of the low voltage side is used. Furthermore, the leakage reactance of the main transformers is used to calculate the impedance of the inductors shown in Fig. 3.3 according to Eq.3.4. Afterwards, this value is converted to per unit values using Eq.3.3. With a leakage reactance of 15% this resulted in a impedance value of  $j0.680625 \Omega$ , which is equal to  $j0.0625 \Omega$  p.u..

$$Z_{Im} = \frac{Z\%}{100} \cdot Z_{base} \quad (3.4)$$

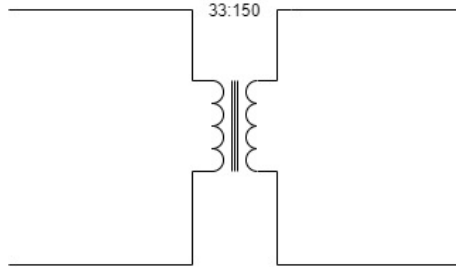


Figure 3.3: 2-winding model for the 3-winding transormers.

## 3.2. Modeling the WTG farm

### 3.2.1. Design of WTG on string level

### 3.2.2. Design of the WTG capability curve

For the WTG, there is a relation between the active output power and reactive output power. In most WTG modeling, the relation is straightforward. The WTG will provide maximum reactive power at all times. With the Enecon Type C used as example [19], this relation is shown in App. A.5 for a voltage magnitude of 1 p.u. When the voltage is unequal to 1, the P-Q relation changes. In addition, some WTGs will produce maximum reactive power, once a certain active power threshold is reached. This condition is shown in App. A.6.

Both cases make the modeling of the output reactive power for the WTG complex. Ideally, from the PQ/RX model, the function for the P-Q relation dependent of the voltage magnitude is calculated [20]. From this derivation the exact output and P-Q relation is determined. However, due to insufficient given data from the case study, the implementation for a PQ/RX model is not feasible. For this reason, the P-Q relation is derived from the Enecon P-Q diagrams of Apps. A.3, A.4, [19].

The procedure to implement the non-ideality of the P-Q relation will consist of determining the equivalent P-Q relation for each WTG generating string in Apps. A.3, A.4. An approximation of this P-Q relation is made by dividing the capability curve in three sections. The first section models the linear slope to reach maximum reactive power at the threshold for the active power. The second section approximates the common case of maximum reactive power. The third section will approximate the decrease of reactive power specified with the slope of a voltage of 0.9 p.u., shown in Fig. A.6. This slope is considered to be a reliable approximation, since it is the closest to the minimum physically allowed voltage of 0.8576 p.u. This prevents a complex implementation of the P-Q relation as a function of varying voltages for each WTG string. Out of this approximation, the wind speed and Q relation is determined and plotted for each generating string in Fig. 3.4. This capability curve will be implemented for every wind speed test model designed in Chap. 4.

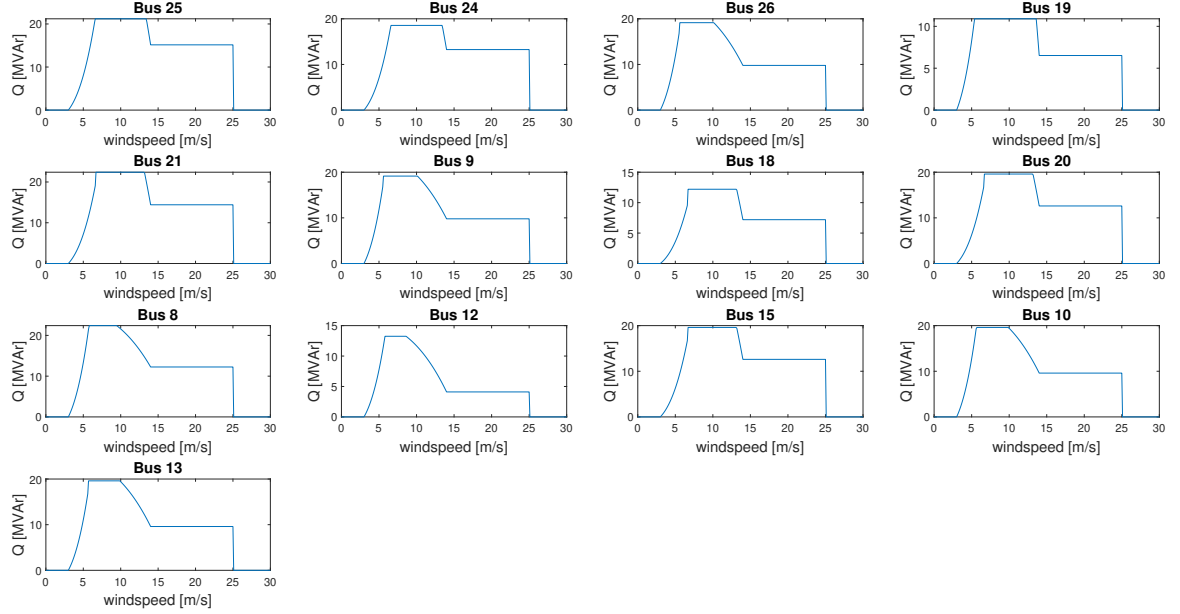


Figure 3.4: Wind speed - reactive power output relation for the WTGs connected in App. 1.1.

### 3.3. Design of the solar farm

#### 3.3.1. Determination of solar farm parameters

For the design of the solar farm, there was no data supplied. This offered a degree of freedom in the design. A rule-based approach is used for the design of the farm.

Firstly, the active power generation of the solar farm is determined. The generation is determined by analysing the weak components of the system. Weak components are considered to be the components, which will have apparent power overloading when running the powerflow. In this case study the weak components are considered to be the transformers and the cable to the PCC. In order to prove this, these components are analysed with the WTG farm generating active power at rated wind speed. The results of this analysis are shown in Figs. 3.6, 3.5 and 3.7.

In Figs. 3.6, 3.5 and 3.7, it can be seen that for the case study used, the branch to the PCC is the weakest component. As can be seen in Fig. 3.7 a capacity of 38.2 MW can be added before reaching the branch limit of the cable. Thus, for each solar farm string an rated power generation of 12 MW is chosen. Therefore, some parts of the day the cable to the PCC will be overloaded with 8 MW. This overloading is needed to give power flow control scheme, the opportunity to come up with solutions in order to guarantee stability and reliability of apparent power at the PCC.

Additionally, the type of solar modules has to be chosen. It was decided to implement the Sunpower X-Series solar modules, because these modules have a high efficiency of 22.2%, in comparison to the average solar

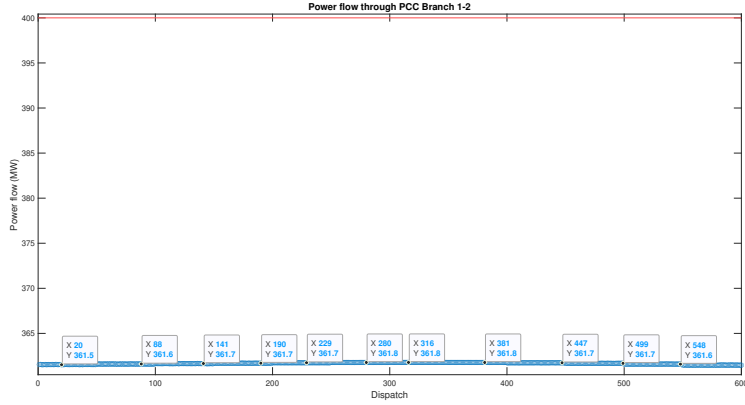


Figure 3.5: Branch limit of the cable to the PCC

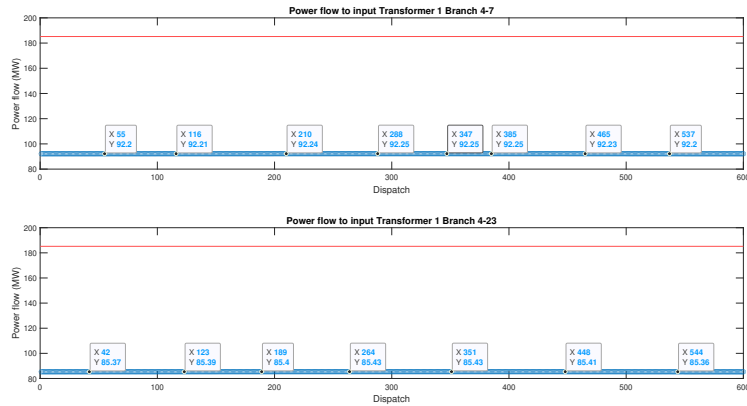


Figure 3.6: Branch limits of the cable to the first main transformer

modules efficiency of 18%, and a sufficient amount of data about the modules is available online [22]. Secondly, because of the AC powerflow in the case system shown in App.A.1, the DC power generated by the solar modules has to be converted into AC power. [24]. Thus, in each photovoltaic string, DC/AC inverters are implemented in order to apply this conversion. However, during this conversion, reactive power is generated by the DC/AC inverters [24]. As shown in [1], the efficiency of this conversion is 98,7%, which will be taken into account when calculating the maximum output power. Since no data of the P-Q capability curves for these solar modules is available, a popular approximation used in research was used for Q, as shown in Eq. 3.5 [7].

$$Q_{gen} = \frac{1}{3} \cdot P_{gen} \quad (3.5)$$

Afterwards, the irradiance in  $W/m^2$  of the location is examined using [5]. When implementing the irradiance profile, a summer model is chosen. This choice is made, since in the summer the irradiance has less fluctuations due to less uncloudy and the highest in comparison to the other seasons. This research resulted in a rated irradiance of  $800 W/m^2$ . This value is used in order to calculate the number of modules needed for each solar farm. As can be seen in [22], the output power of each module at Standard Test Conditions (temperature of  $25^\circ C$ , irradiance of  $1000 W/m^2$  and an air mass of 1.5 (AM 1.5) is 360W. For the sake of simplicity, the output power is considered to be linearly dependent with the irradiance. Thus, the other two variables, temperature and air mass, are not considered to be of influence in this model. With this assumption, the output power of each module is calculated by Eq. 3.6.

$$P_{module-location} = \frac{I_{location}}{I_{STC}} \cdot P_{module-STC} \quad (3.6)$$

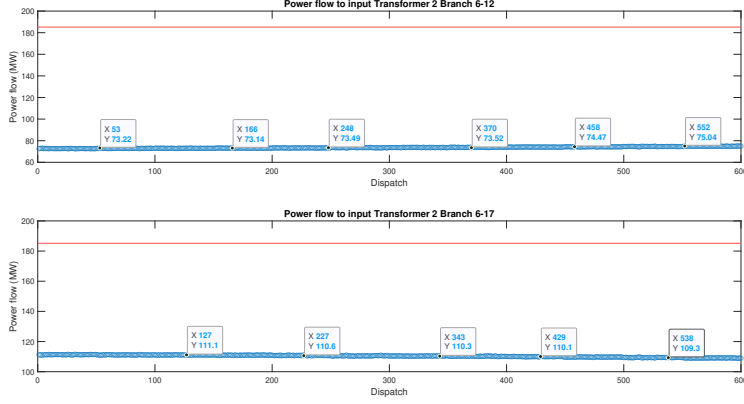


Figure 3.7: Branch limits of the cable to the second main transformer

$$N_{modules} = \frac{12 \cdot 10^6}{P_{module-location}} \quad (3.7)$$

In addition, the amount of solar modules needed is calculated by Eq. 3.7. These calculations resulted in 41667 solar modules for each photovoltaic string.

Table 3.3: Maximum output current and voltage of one solar module [22]

Maximum Output voltage	69.5 V
Maximum Output current	6.48 A
Bus limit	36kV
Branch limit	1402.96 A

### 3.3.2. Solar farm overview

Additionally, the interconnection of the solar modules is determined by considering the capacity limits of the bus bars to which these photovoltaic strings are connected. An interconnection as shown in Fig. 3.8 is chosen, since this interconnection will not violate any voltage or current bus/branch limits [15]. In Fig.3.8, 204 solar modules are connected in series per array, which results, using Kirchhoff's voltage law and 3.3, in a maximum output voltage of 14,178 V for each array. This voltage has to be transformed to the base voltage of the bus bar in order to connect to the grid. Therefore, a 14 kV/33kV transformer is connected as shown in Fig. 3.8. On the other hand, 205 arrays are connected in parallel, which results, using Kirchhoff's current law and 3.3, in a total maximum current of 1328 A for each photovoltaic string. The last consideration that had to be made is that the inverter has a limited number of inputs, i.e. three inputs. Therefore, sub array connectors are used in order to connect the arrays with the inverter.

Eventually, the cable length from the interconnection point to bus bars is approximated by examining the data of the location and the cable lengths of the WTG strings. This resulted in the approximated length shown in App.A.1.

## 3.4. Method to determine model accuracy

MatPower solves the power flows, voltage/current profiles and power losses of nodes in the system, using the Newton Raphson method [23]. To determine if the model was implemented correctly and MatPower is a reliable source tool, the same method was applied with hand calculations. Hereby, the same setpoints for generating strings used for the MatPower code were used to solve the iterative power flow.

Since the system configuration consists of 28 bus bars and 17 generating strings, it could be concluded that performing hand calculations on the entire system would be too intensive for the purpose of this project. Therefore, it was decided to perform the calculations for one string. This comparison is done for two different reactive power setpoints. The strings chosen were based on the known parameters of the system. When

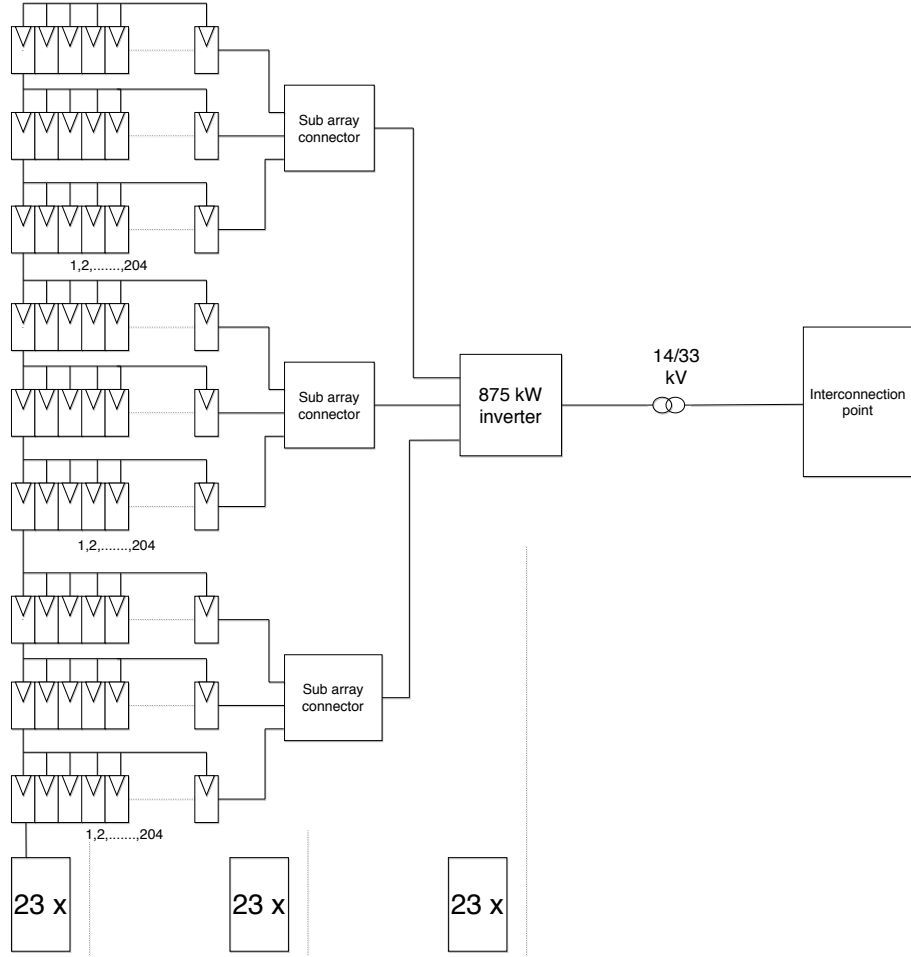


Figure 3.8: Overview of solar farm design

there is a PCC request, reactive power setpoints are sent to the generating strings from the slack node top, to the strings down. Based on this, the voltage profile and current is best known between the WTG and connected bus, e.g. the power flow of branch 7-8 with bus 8 being the WTG, is known after the reactive power demand is known at bus 7. To choose which branch is most relevant to model, the longest branch was chosen since this will cause a higher voltage difference and power loss in the string. With a length of 7561 m, branch 23-24 is tested.

Firstly, an equivalent test model is made for the branch, shown in Fig. 3.9. After, an equation is formulated for the active and reactive power through branches Eq. 3.8 and Eq. 3.9. In these equations,  $i$  will be the node for which the power is unknown and  $n$  will be the node with known magnitude and angle values.  $Y_{in}$  is the admittance value in the admittance matrix for the branch between node  $i$  and  $n$ . With the Jacobian of Eq. 3.10, Eq. 1.4 is solved. From Eq. 1.4, the power flow is determined. If the mismatch between the calculated power flow and the desired power flow is below a certain threshold, the vector of Eq. 1.4 yields the final solution.

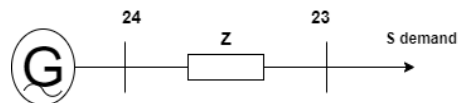


Figure 3.9: Equivalent test model of branch 23-24

$$P_i = \sum_{n=1}^N U_i \cdot U_n \cdot Y_{in} \cdot \cos(\delta_i - \delta_n - \theta_{in}) \quad (3.8)$$

$$Q_i = \sum_{n=1}^N U_i \cdot U_n \cdot Y_{in} \cdot \sin(\delta_i - \delta_n - \theta_{in}) \quad (3.9)$$

$$\begin{vmatrix} \frac{\partial P_i}{\partial \delta_i} & \frac{\partial P_i}{\partial U_i} \\ \frac{\partial Q_i}{\partial \delta_i} & \frac{\partial Q_i}{\partial U_i} \end{vmatrix} \quad (3.10)$$

To solve the equations, all values will be in per unit. To arrive at the known parameter values, the MatPower code A.4.1 is ran with random setpoints centered around 0 and maximum active power generation for each strings. From this test, the values in Tab. 3.4 are determined. Using Fig. 3.9, in the first test it is assumed that the generation is known, i.e. at bus 24, and the voltage profile at bus 23. In the second test the apparent power demand is known, i.e. at bus 23, and the voltage profile at bus 24. In this manner, the Newton Raphson method is applied for both sides of the model, yielding a more reliable hand calculations result.

Table 3.4: MatPower known parameters for the model of branch 23-24

Bus number	Voltage magnitude (p.u.)	Voltage angle (degrees)	Y admittance (p.u.)	P (p.u.)	Q (p.u.)	P loss (MW)	Q loss (MVA)
23	0.9801	18.5814	1.265 - j 7.216158756	0.294	0.000169	0.0607	0.3465
24	0.9776	19.2510	1.265 - j 7.216158756	0.294	0.00023	0.0607	0.3465

For the purpose of this project, a threshold of 0.0001 p.u. for the power flow mismatch is chosen, which is recommended in the lectures of the supervisor for the project. After the final solution is found from Eq. 1.4, the current magnitude and angle is determined. Using Ohm's law, the active and reactive power losses are calculated. Then, the mismatch between the MatPower and hand calculations is analysed to determine if this mismatch can be neglected for the purpose of this project. Based on the total active power, 400 MVA, that theoretically could be provided at the PCC (Bus 1), a maximal mismatch of 1 MW for active power and 1 MVA for reactive power is chosen. The relative mismatch is 0.25 % which is considered to be a negligible inaccuracy. Furthermore, this mismatch is well within the allowable deviation of the PCC request [19]. The hypotheses is that if the MatPower results are sufficiently close to the hand calculations, MatPower modeling proves to be accurate.

### 3.4.1. Comparison to other Power Flow solving methods

# 4

## Test models for operating conditions

To determine the system behaviour after each system update, different Operating Conditions (o.c.) were designed. System updates occur when the dispatch profile is known, i.e. wind speed ( $m/s$ ) and solar irradiance ( $W/m^2$ ). Furthermore, the system is updated after receiving setpoints for generating strings. The setpoints indicate if a certain string is required to be connected and deliver apparent power and what the amount is that shall be delivered, this relation is shown in Fig. 2.1. The results of these test models yield the relation between dispatch profiles, losses in the system and setpoints received from the PCC.

$$P_{output} = P_{rated} \cdot \frac{v_{wind}^3 - v_{cutin}}{v_{rated}^3 - v_{cutin}} \quad \text{for } v_{cutin} < v_{wind} \leq v_{rated} \quad (4.1)$$

$$P_{output} = P_{rated} \quad \text{for } v_{rated} < v_{wind} \leq v_{cutoff} \quad (4.2)$$

$$P_{output} = 0 \quad \text{elsewhere} \quad (4.3)$$

After defining what parameters shall be tested, the relevant o.c. should be determined for the transmission system. This can be divided in normal o.c. and extreme o.c. Normal o.c. is defined by the most frequent PCC setpoint request at a nominal dispatch profile. Following from [19], normal setpoints are defined by the request of maximum active power output (MW) and zero reactive power (MVar). Consequently, in most cases the power factor requested at the PCC is equal to 1. Furthermore, nominal dispatch profiles are defined by  $v_{wind} = 7.5m/s$  and  $I = 500W/m^2$ . Using Eqs. 4.1, 4.2, 4.3 and Eq. 3.6 the active power output is computed for WTG and photovoltaic strings. Using Fig. 3.4 and Eq. 3.5, the reactive power output is computed. It can be seen from Eq. 4.1, that a nominal wind speed will not give maximum active power output. However, from Fig. 3.4 every WTG string will generate maximum reactive power. The rated power for each string is found in App. A.3 and A.4.

Therefore, extreme o.c. are defined for setpoints of which the power factor is lowest for a specific dispatch. The power factor is given by Eq.4.4.

$$pf = \frac{P}{\sqrt{P^2 + Q^2}} = \frac{P}{|S|} \quad (4.4)$$

From Eq.4.4 can be derived that the lowest power factor is reached when the maximum positive or negative reactive power that the string can deliver, is requested from the PCC. For the extreme test models, this behaviour is analysed for a very low P generation and a very high P generation of the connected strings. To determine the dispatches corresponding to realistic low P generation and high P generation, probabilistic distribution for wind profiles is run with parameters from the case study [19]. For the solar profiles it is based on the historical data of the case study [5].

There might be concerns about the Q requests made by the PCC, leading to a violation of the rated apparent power of the branches, explained in Sec. 3.1. Therefore, a quick calculation was made to determine the maximum apparent power flow through the branches.  $P_{max} = 33MW$  and  $Q_{max} = 22.4MVar$ , therefore

$S_{max} = \sqrt{(33)^2 + (22.4)^2} = 39.9\text{MVA}$ . This is below the rated apparent power limit, i.e.  $46.2977\text{MVA}$ , of the branches and can therefore be neglected for the test models designed.

Since the load demand is unpredictable in realistic situation, it was decided to apply a normal distribution with a standard deviation of 8 % from the maximum reactive power output [4]. The mean of the distribution is calculated by dividing the reactive power at the PCC by the amount of connected generating string. This reactive power is swept from the maximum negative reactive power to maximum positive reactive power in certain steps. It is believed that by doing this sweep, it will be able to derive relations between the voltage magnitude and active/reactive power losses or reactive power injections in the system.

It should be noted that for each wind/solar dispatch design, it is assumed that the uncorresponding renewable energy system is inactive. For example, when the photovoltaic power generation is modeled with the designed solar irradiance daily dispatch, the WTGs are considered to be disconnected. The same counts for the wind daily dispatch design and the disconnected PV module. Once each design is tested individually, the dispatches can be combined in a normal random distribution function for wind-and solar power connected simultaneously.

To test the system behaviour, the model is tested under different operating conditions. A total of 300 dispatches are made, i.e. 15 minute dispatches [4]. More dispatches will be confusing to analyse and less will be insufficient data. For the correctness of the tests, it is important to disconnect or neglect components that are not part of the components of interest.

For each test model the procedure explained in Fig. 4.1 will be followed. It is divided in different sections that make it possible to derive conclusions in a stepwise manner. Firstly every relevant system and test parameters are calculated and implemented in order to run power flows.

Out of the power flows the data is processed to make relation plots and data vectors indicating violation of voltage magnitudes constraints. The voltage limitations are shown in Tab. 4.1. The constraints are based on the voltage limitations of the transformer inputs, i.e. bus 4 and 6 of Fig. A.1. Lastly, these plots are used again to compare it to other test models results.

Especially, the 3-D plots make data analysis more manageable. For each dispatch, the total system behaviour is plotted for different dispatches. Out of this comparison it can be concluded if expectations are satisfied.

Table 4.1: Voltage constraints for the transmission system

Minimum allowed voltage (p.u.)	Maximum allowed voltage (p.u.)
0.8576	1.1424

## 4.1. Hypotheses on results

### 4.1.1. Active and reactive power losses

As is already known, the PCC generates reactive power demand from the generating strings. This situation can be reformulated by a simplified AC model shown in Fig. 4.2 and Fig. 4.3. When the demand at the PCC is positive, the PCC behaves as an inductive element, for which  $X = j\omega L$ . Fig. 4.2 shows that when this is the case, the voltage at bus bar 1, i.e. the PCC, is the negative terminal of the reactance. Therefore, the average voltage magnitude of the transmission system, i.e. the positive terminal, must be higher than bus bar 1 to satisfy this behaviour. For a capacitive element, for which  $X = \frac{-j}{\omega C}$ , the opposite relation applies. The average voltage magnitude, i.e. the negative terminal, must be lower than bus bar 1. The PCC was considered to be the slack node with 1 p.u. and 0 angle degrees, explained in Chap. 3. From this relation it can be concluded, the more positive the reactive power demand, the higher, above 1 p.u. the average voltage will be. The more negative the reactive power demand, the lower, below 1 p.u. the average voltage.

Out of the relations described by Figs. 4.2 4.3, also the voltage-loss relation of the system could be derived. Eqs. 4.6 4.7 describe a parabolic relation between the parameters, mirrored in the x-axis around the voltage

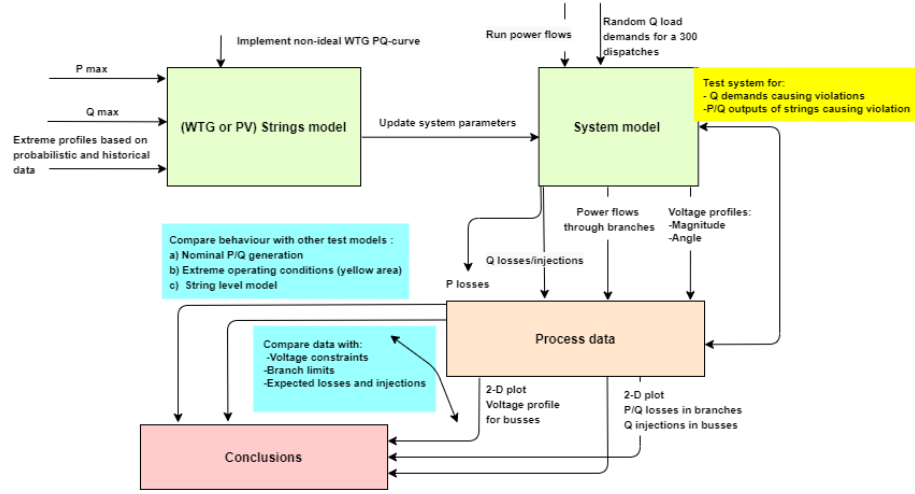


Figure 4.1: Overview of procedure to derive conclusions.

of the slack node. One should notice that the Eqs. 4.6 4.7 are multiplied with the voltage base squared, otherwise the losses were in per unit values.

Although, a parabolic relation is described, the reactive power demand strongly influences which part of the graph is extended in losses. Same demands, but of opposite sign have other effects on the losses. Using the simple Eq. from Ohm's Law 4.5, it is expected that negative demands of equal magnitude to its equal positive demands, will cause more losses in the system. Since Ohm's Law must be satisfied for all circumstances, when  $\delta V = V - V_{slack}$  is higher for negative demands, the current through the branches of the system becomes higher to still satisfy the power flow through the system. Because of this higher current, there will be more dissipation through the impedances of the branches, causing higher losses.

Ideally the slack voltage is 1 p.u., but this value inserted can slightly deviate if the Newton Raphson solves the power flow with a different vector solution in Eq. 1.1. This is caused by a small power mismatch.

$$V = I \cdot Z \quad (4.5)$$

$$P_{loss} = \frac{(V - V_{slack})^2}{R} \cdot (V_{base}^2) \quad (4.6)$$

$$Q_{loss} = \frac{(V - V_{slack})^2}{X} \cdot (V_{base}^2) \quad (4.7)$$

#### 4.1.2. Reactive injection losses

The expected relation for the average voltage and losses due to injections in the bus bars, is explained by Eq. 4.8, with Q reference = 0 MVA. This was relation was derived from [17] and shall be consulted for further explanation. Here, it was assumed that the injection losses are equivalent to the reactive power present by droop losses. Eq. 4.8 describes a linearly increasing reactive injection for decreasing voltage transmitted to the PCC. This relation is expected for every test conditions. Furthermore, it will not change for different generations of the same system model, since the droop coefficient does not change. It stays constant and therefore the same relation holds.

#### 4.1.3. Reactive power demand

To derive the exact relation between total reactive power demand by the PCC and the average voltage of the system, [12] suggested an analysis of an exponential load model. The exact parameter values that describe the relation described by this load model is yet unknown. This will be derived from the results in Chap. 5. However, it is expected that the same relation is held for every test model analysed.

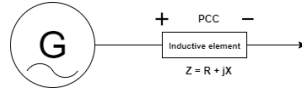


Figure 4.2: PCC behaves as an inductive element.

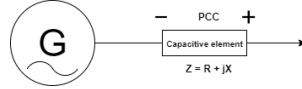


Figure 4.3: PCC behaves as a capacitive element.

$$Q_{\text{injected}} - Q_{\text{reference}} = -\frac{1}{R_u} \cdot (V_{\text{transmitted}} - V_{\text{slack}}) \quad (4.8)$$

#### 4.1.4. Expected system behaviour

Following from the relations described above, it was concluded that the power flows through the system directly influence the voltage magnitude and losses. Therefore, the higher the total active power generation, the higher the active power losses. The order of available generation for the farms is from solar farm (40 MW), to wind farm (363 MW), to hybrid farm (403 MW). Concluding, in the same order the active power losses will increase. Furthermore, active losses and reactive losses have a linear relation.

However, using Fig. 3.4 and Eqs. 4.1, 4.2, notice that for higher active power generation of the system, the reactive power generation is lower for WTG strings. Thus, the apparent power is decreased. If the total apparent power for a higher active power generation becomes lower than that of nominal active power generation, the conclusion is changed for reactive losses. Nominal conditions active power generation will have more reactive losses than active power generation, since the available reactive demand is highest. The influence this will have on the expected sequential order for losses of farms compared to each other, is yet unknown. This is discussed in Chap. 5.

## 4.2. Wind farm procedure

For the wind farm, the solar farm will be disconnected. The procedure of Fig. 4.1 is followed for three different wind speeds, one of them being the nominal wind speed, i.e. 7.5 m/s.

The choice of the wind profiles was based on a Weibull PDF. Out of data for the case study, the scale parameter, 2.54 p.u. and shape parameter, 7.86 m/s was found [19]. With these parameter, the probability for extreme wind speeds was determined. By running 1000 samples of the Weibull PDF, the probability of the chosen wind speeds is analysed. In Tab. 4.2, it is found that the probability to be at extreme wind speeds is relatively high, namely approx. 10 % of the times. This probability is higher for windy seasons, making its inspection relevant. The wind speeds chosen were close to the cut in and cut off speed boundaries. For extreme low generation it was decided to choose 4 m/s. For extreme high generation this was 14 m/s. From Eq. 4.2, will generate maximum at this chosen wind speed.

Table 4.2: Probability of extreme wind speeds for the location of the case study.

V low (m/s)	Probability of exceeding V	V cut in (m/s)	V rated (m/s)
4	0.135	3	14
V high (m/s)	Probability	V cut off (m/s)	V rated (m/s)
13	0.016	25	14
14	0.07	25	14

As explained in the Sec. 4.1, the mean of the normal distribution for load demands will be swept from maximum negative reactive power to maximum positive reactive power. The average maximum of the WTG strings is calculated by summing the reactive power at nominal wind speed(7.5 m/s) using Fig. 3.4, yielding 18.46 MVAr. For a correct behaviour analysis from different sample points as means, it was decided to sweep this mean in 20 steps, from 18.46 to -18.46 MVAr. 20 steps is considered an estimate for sufficient means to

yield plots that show a relation between in the 3-D plots. Since the generation of reactive power is lower for extreme wind speeds, the means and subsequently, the sample points in the 3-D plots will be closer to each other, making the plots unreadable if a higher amount of dispatches is used, strengthening the argument of using 300 dispatches for analysis [9].

To test the effect the shunt reactor component has on the system behaviour, a test will be run for which the shunt reactor is connected at nominal wind speed. Although the shunt reactor is connected, the same reactive power setpoints are sent by the PCC to the WTG strings, as done for the test models with shunt reactor disconnected. By doing this, the difference between the results of the test models, will solely indicate the effect of the shunt reactor.

### 4.3. Solar farm procedure

In order to test the behaviour of the solar farm solely, the wind farm is disconnected before running the test models. The procedure shown in Fig. 4.1 is executed for three different solar irradiances.

As described in Subsec. 3.3.2, the solar profile is implemented for summer days and is based on historical data. Additionally, the normal and extreme o.c of the photovoltaic strings have to be determined. This done by examining the solar irradiance of the location assigned for this project. Furthermore, the irradiance is modeled in a discrete manner, meaning that a certain irradiance is modeled for the whole day. This is not an optimal modeling of the reality, because the sun radiation increases in a stepwise manner during the day. However, this can be justified, since the emphasis of these tests is on testing the capability of the system in dealing with extreme conditions.

For the extremely low o.c the minimum irradiance of the location is taken. The same is done for extremely high o.c. For the normal operating condition, the average and most common irradiance is taken [5]. The results are shown in Tab. 4.3. In order to determine and implement the random load demands the same procedure is used as for the wind farm as described in Sec. 4. The same procedure as described in Sec. 4.2 is used in order to determine the average maximum of the Q demands of the photovoltaic strings. This resulted in an average of 10 MVAr. For a correct behaviour analysis from different sample points as means, it was decided to sweep this mean in 10 steps, from 10 to -10 MVAr. For the photovoltaic strings 10 steps are considered to be sufficient menas to yield plots that show a relation in 3-D plots. The same reasoning as for the windfarm tests is used in order to justify the amount of steps. The complete elaboration can be found in Sec. 4.2.

Table 4.3: Normal and Extreme o.c of the photovoltaic strings [5].

Category of operating condition	Irradiance [ $W/m^2$ ]
Extremely Low	100
Normal	500
Extremely High	800

### 4.4. Hybrid farm procedure

Eventually, the wind farm and solar farm are both connected to the system configuration in App. 1.1. The procedure described in Secs.4.2, 4.3 were combined in order to test the behaviour of the hybrid farm. The extreme conditions of wind as described in Sec.4.2 are combined with those of solar, which were elaborated in Sec. 4.3. For normal operating conditions the same procedure is implemented. This total of three operating conditions with subsequent dispatch profiles are shown in Tab. ???. The results of these test models will be further elaborated in Subsec. 5.2.4.

Table 4.4: Three operating conditions are tested to determine the system

	Wind farm speed (m/s)	Solar irradiance (W/m2)
Low generation	4	100
Nominal generation	7.5	500
High generation	14	800

# 5

## Results

### 5.1. Determination of model accuracy

After the Newton Raphson method was applied to the test model of Fig. 3.9, interesting observations were made. Firstly, it was found that unless the first initial guess of the unknown voltage magnitude and angle is close to the final values for Vector 1.1, the Newton Raphson method would not converge in less than 10 iterations. This behaviour is shown for first test in Tab. 5.2, for which the voltage at bus 24 and power demand of bus 23 are unknown. After the first few iterations, the voltage magnitude and degrees would be further away from the final answer. An alternative had to be searched to prevent complex hand calculations for a calculation that can be simplified.

Any power flow calculation done that requires more than 10 iterations, is considered to be too complex to solve with the hand [23]. Moreover, the calculations were performed for solely one branch. If the power flow was tried to solve for a test model of a greater section of the system in App. 1.1, the complexity would increase and therefore the required time to solve. Because of this complexity it was decided to make an own MatLab code for the hand calculations of NR-method found in App. A.4.1. This code will yield the final answer and amount of iterations immediately. Secondly, it was found that the threshold of 0.0001 p.u. for the power mismatch was not feasible for hand calculations. In most cases the system would not converge. It was decided to increase the allowable power mismatch to 0.1. After this was done, the NR would converge in some cases. In Tab. 5.2 the results are shown and the indication of the initial guess. The smallest power mismatch is found when the first initial guess is  $V = 1\angle 20$ . A similar test was performed to determine if the voltage at bus 23 could be calculated, as well as the power generation of bus 24. Using the results of Tab. 5.3, the smallest mismatch is when the initial guess is  $V = 0.97\angle 20$ .

Table 5.1: Hand calculations for test 1; voltage profile at bus 24 is solved. Voltage of bus 23 and power generation at bus 24 are known parameters.

Iter.	V guess (p.u.)	$\angle$ guess (degrees)	V result (p.u.)	$\angle$ result (degrees)	P mismatch (p.u.)	Q mismatch (p.u.)
1	1	0	0.9465	-22.7570	N.A.	N.A.
2	1	0	0.3053	-110.6236	N.A.	N.A.

Table 5.2: Hand calculations with code of App. A.4.1 for test 1; voltage profile at bus 24 is solved. Voltage of bus 23 and power generation at bus 24 are known parameters.

Iter.	V guess (p.u.)	$\angle$ guess (degr.)	V results (p.u.)	$\angle$ results (degr.)	P mismatch (p.u.)	Q mismatch (p.u.)	Converged
256944	1	0	0.9465	-22.7570	2.4503	-0.9096	No
294631	1	10	0.9983	-1.0222	1.3063	-0.4098	Yes
1	1	20	1.0157	19.0616	0.0928	-0.1162	Yes
1645122	0.99	20	0.9959	19.0518	0.1074	N.A.	No
1	0.996	20	1.0078	19.0577	0.0987	N.A.	Yes

Table 5.3: Hand calculations with code of App. A.4.1 for test 2; voltage profile at bus 23 is solved. Voltage of bus 24 and power demand at bus 23 are known parameters.

Iter.	V guess (p.u.)	$\angle$ guess (degr.)	V results (p.u.)	$\angle$ results (degr.)	P mismatch (p.u.)	Q mismatch (p.u.)	Converged
126514	1	0	0.9820	-22.7570	1.9422	-0.9262	No
156329	1	10	1.0203	-1.0222	0.8010	-0.4264	No
3392753	1	20	1.0258	19.0616	-0.4120	-0.1329	No
867535	0.99	20	1.0062	23.0715	-0.3982	-0.0555	No
835672	0.97	20	0.9665	23.1346	-0.3715	0.0856	No
2367897	0.97	19	0.9673	21.1310	-0.2517	0.0650	No
2	0.97	16.5	0.9679	16.1265	0.0461	0.0044	Yes

The results are compared to the results of MatPower, having a noticeable margin of error in either the MatPower or the hand calculations results. For the voltage magnitude and angle the difference seems to be minimal. However, in Tab. 5.4 it can be seen that the hand calculations give higher P and Q losses in the branch. Several explanations were found to explain this difference for  $\Delta P = 0.1318\text{MW}$  and  $\Delta Q = 0.7513\text{MVA}_\text{R}$ . It should be noted that these values are within the maximum allowed power difference of 1 MW and 1 MVA<sub>R</sub>, explained in Sec. 3.4. Since MatPower also makes use of the NR-method to solve the power flows, it was decided to analyse how MatPower applies this method [28]. The threshold MatPower uses by default is significantly lower, namely  $10^{-4}$ , making the final solution 1.1 more accurate by yielding smaller power mismatches. Ideally, this is closest to 0 to satisfy Eq. 1.5. Thus, the hand calculations yields less satisfactory results with power mismatches close to the high threshold of 0.1. Secondly, MatPower considers the angle shift caused by the branch model in Fig. 3.1 when calculating losses. Therefore, the losses are defined as shown in Eq. 5.1 [28]. This was something that could not be taken into account for the hand calculations. Lastly, MatPower ran the power flow the case study, while for the hand calculations only one branch of the 31-branches system was tested. Thus, the influence the power flows of other branches have on the branch analysed in Fig. 3.9 cannot be considered for hand calculations.

$$\text{Losses}_{\text{branch}} = \frac{\left| \frac{V_{from}}{re^{j\theta_{shift}}} - V_{to} \right|^2}{Z_{\text{branch}}} \quad (5.1)$$

The hand calculations were performed to determine if the MatPower implementation was done correctly. However, it could be concluded that hand calculations are a less accurate approximation for several reasons. Due to the complexity, mistakes are easier to be committed. Furthermore, hand calculations use rougher approximations to converge for the power flows, since the threshold could be considered high for the purpose of this project and the fact that the influence of other branches were not considered. Concluding, MatPower is an open source-tool that gives more satisfactory solutions, as well as faster. Therefore, system of this scale, 28 bus bars and 31 branches, are recommended to solve with MatPower or other algorithms available with low threshold and fast convergence. The  $\Delta P/Q$  in Tab. 5.4 lied within the allowed limits. Hence, hand calculations are not a wrong approximation, were the system power flows solved completely by this methodology.

Table 5.4: Results for voltage profile and losses are compared for MatPower and hand calculations.

	V bus 23 (p.u.)	$\angle$ bus 23 (degr.)	V bus 24 (p.u.)	$\angle$ bus 24 (degr.)	P losses branch 23-24 (MW)	Q losses (MVA <sub>R</sub> ) branch 23-24
MatPower	0.9776	18.5814	0.9801	19.2510	0.0607	0.3465
Hand	0.9679	16.1265	1.0157	19.0616	0.1925	1.0978

### 5.1.1. Comparison to other Power Flow solving methods

## 5.2. Test Models for operating conditions

After completing the implementation of the test models for each farm, the different test models are run and the results are analysed. During this analysis, the results for each farm are inspected to determine the satisfaction of the hypotheses made in Sec. 4.1.

Firstly, the 3-D plot is made by plotting the parameters of interest against each other. For every operating condition:

1. On the Y-axis: the active power losses/ reactive power losses.

2. On the X-axis: the reactive power demand
3. On the Z-axis: the average voltage magnitude of the system.

This plot is generated in order to prove whether the relationship described in Eq.4.6 is satisfied. The same procedure is done for the reactive power losses in order to prove whether the relationship described in Eq.4.7 is satisfied. Secondly, the losses on the Y-axis are replaced by the reactive power injections. This plot is generated in order to prove whether the relationship described Eq. 4.8 is satisfied. Eventually, the relation between the setpoints Q and the average voltage of each dispatch is inspected.

### 5.2.1. Wind farm

**Active and reactive power losses.** The test models for the wind farm were run for the three o.c., as described in Sec. 4.2. The result of this test is shown in Fig. 5.1. In Fig. 5.1, the quadratic relation is seen between the active power losses and voltages approximately centered around  $V = 1.0$  p.u., as described in Eq.4.6. This is satisfied for all wind speeds. The peak of the parabolas shown in Fig.5.1 is defined as the voltage for which the active power losses reach the minimal value. This is because the system is considered to be most stable when the average voltage is equal to the voltage of the slack node, i.e. 1 p.u. Ideally, this peak corresponds to the normal o.c. Hence, the PCC in Figs. 4.2, 4.3 will behave solely as a resistive element. In such case, the reactive demand is 0 MVar. Hence, the expected minima coordinates were **minima = [minimum loss value 0 1]**. However, the power flows are not solved analytically, for which there is an unspecified insignificant margin of error for the final solution of Eq. 1.1. Therefore, the parabola is centered around other coordinates than initially expected. For the dispatches ran for  $v = 7.5m/s$ , **minima = [0.02667 -18.1 1.001]**, for  $v = 14m/s$ , **minima = [1.02 15.92 1.006]**. The width of the parabolas are reasonably wide. This compensates for this error, since the loss value for a reactive demand of 0 MVar, its deviation for P ranges from  $|0.00346| < \Delta P < |0.004| MW$ . For Q this deviation ranges from  $|0.14| < \Delta Q < |0.179| MVar$ . Concluding, this deviation is so small that can be neglected. The ideal coordinates can be assumed. Therefore, it can be concluded that for each o.c. setpoints of  $Q = 0$  MVar result in the lowest losses.

Fig. 5.1 depicts that the higher the available reactive power generation and subsequently, allowable total reactive power demand, the more the graph is extended for a certain wind speed. For the nominal wind speed  $v = 7.5m/s$ , the graph is the most extended, since Fig. 3.4 shows that the strings generate maximum reactive power. Using Fig. 3.4, for  $v = 14m/s$  reactive power generation is less and for  $v = 14m/s$  the least. Concluding, the non-ideal capability curve explained in Sec. 3.2.2 was implemented correctly, improving the accuracy of the model.

Fig. 5.1 shows that the higher the active power generation (e.g. the higher the wind speeds), the higher the active power losses. This satisfies Ohm's law described in Eq. 4.5, since higher active power generation results in higher currents, which give rise to higher losses in the branches. The exact numbers are shown in Tab. 5.6. Furthermore, for normal and high o.c. Fig.5.1 shows that voltages lower than 1.0 p.u. result in higher losses than voltages higher than 1.0. p.u. Eq. 4.5 clarifies this observation. For a constant impedance, voltages higher than 1.0 p.u. result in lower currents. Therefore, the active power losses will be lower. As higher wind speeds will cause a higher power flow, which will lead to a higher current, this influence becomes larger for higher wind speeds as shown in Fig.5.1. On the other hand, low wind speeds will cause such a low power flow that the influence of the difference in active power losses between  $V_{max}$  and  $V_{min}$  is negligible as shown in Tab. 5.5. In conclusion, the influence of higher power flow on the losses is only satisfied for the normal and high o.c..

An interesting observation made in the result was that for the nominal wind speed, the parabolic relation seems to be most symmetric. A Q demand of same value, but opposite sign will cause approximately the same amount of P/Q losses. This is seen by the highest and lowest X-values of the blue graph in Fig. 5.1. This is not satisfied by the extreme wind speeds. However, for low wind speeds it can be neglected due to the minimalist magnitude of the losses. As explained in the paragraph above, Eq. 4.5 will cause higher losses for low voltage profiles. Therefore, the relation between voltage and P is symmetric, but does not extend equally. A similar positive or negative power demand causes an equal deviation from the  $V_{slack}$  for the voltage, but this voltage will cause higher losses if it is below  $V_{slack}$ . The reason for this symmetry solely for nominal wind speed cannot be explained. One possible explanation could be that the nominal wind speed is not generating

enough active power to make a significant difference in current generation between positive and negative Q demands, to depict a difference in power loss for lower or higher voltage profiles.

Table 5.5: Difference in active power losses between  $V_{max}$  and  $V_{min}$  for each o.c.

Operating condition	$P_{lossV_{min}} - P_{lossV_{max}}$ [MW]
Low generation (4 m/s)	-0.027303
Nominal generation (7.5 m/s)	0.0311
High generation (14 m/s)	0.155

Table 5.6: Active power losses for different operating conditions.

Operating condition	Maximum active power losses [MW]
Low generation (4 m/s)	0.03588
Nominal generation (7.5 m/s)	0.5019
High generation (14 m/s)	1.269

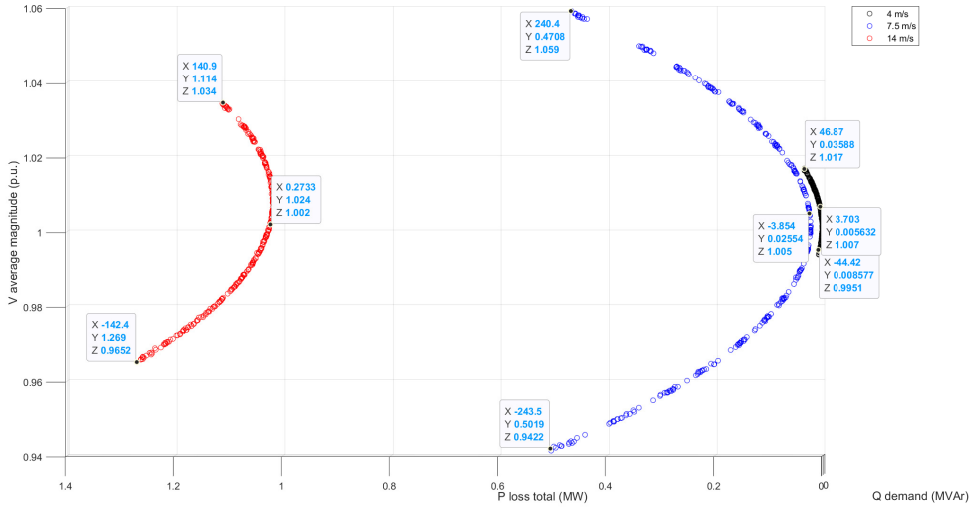


Figure 5.1: 3-D relation of the average voltage magnitude (p.u.), active power losses and random Q demands for the wind farm.

**Reactive power injections.** From the result of Fig. 5.2, a negative linear relation is seen for the three wind speeds, between the voltage magnitude and total reactive injected power. The droop relation described by Eq. 4.8, predicts this behaviour. Furthermore, it is not possible to make a differentiation between the Q-relation for three different wind speeds. This satisfies the hypotheses made in Sec. 4.1, which was explained by the fact that the droop coefficient  $R_u$  does not change for different wind speeds. This coefficient changes if the system configuration changes. Hence, it will change for the solar and hybrid farm results. Additionally, the hypotheses based on Eq. 4.8 stated that the higher the allowable range of reactive power demand, the more the relation is extended between voltage and injection. This is seen in Fig. 5.2 since the blue graph, for nominal wind speed and thus highest  $Q_{range}$  extends the most compared to a smaller extension for the red graph, i.e. 14 m/s and the smallest extension for the black graph, i.e. 4 m/s. The difference between extension for 4 m/s and 7.5 m/s is reasonably small. The max and min for 4 m/s are 38.32 MVar and 36.69 MVar. While for 7.5 m/s this is 39.63 MVar and 34.72 MVar. The generation for reactive power is highest for 7.5 m/s. If the reactive power generation had influence on the injection, the graph would be most extended for this wind speed. However, from Eqs. 4.1, 4.2, the active power generation increases for an increase in wind speed. In conclusion, in a linear relation, the higher the active power flow through the system, the higher the reactive power injections. Lastly, it should be noted that the injections made in the systems are reasonably

high if a maximum demand of 240 MVar is made in the system. Therefore, it will be interesting to inspect the components responsible for such behaviour.

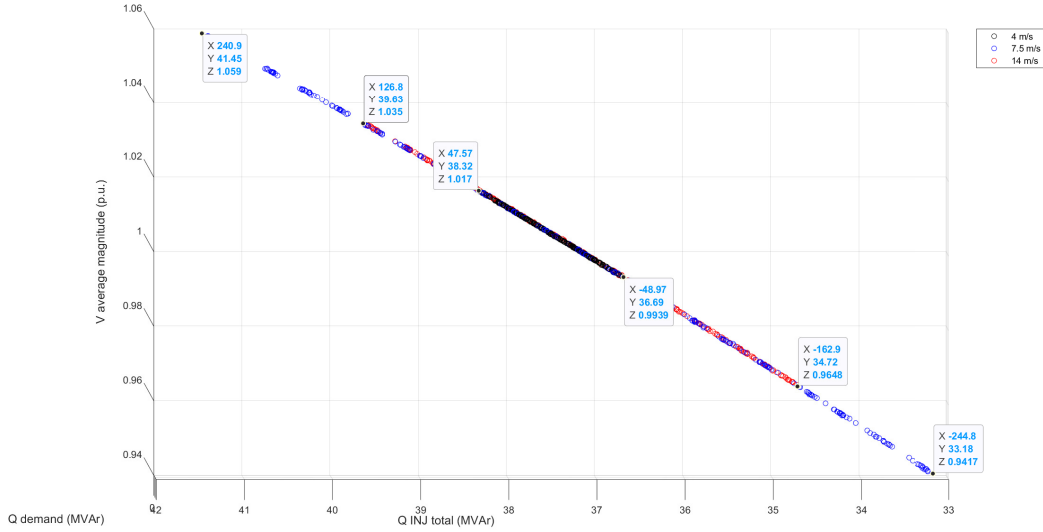


Figure 5.2: 3-D relation of the average voltage magnitude (p.u.), active power losses and random Q demands for the wind farm

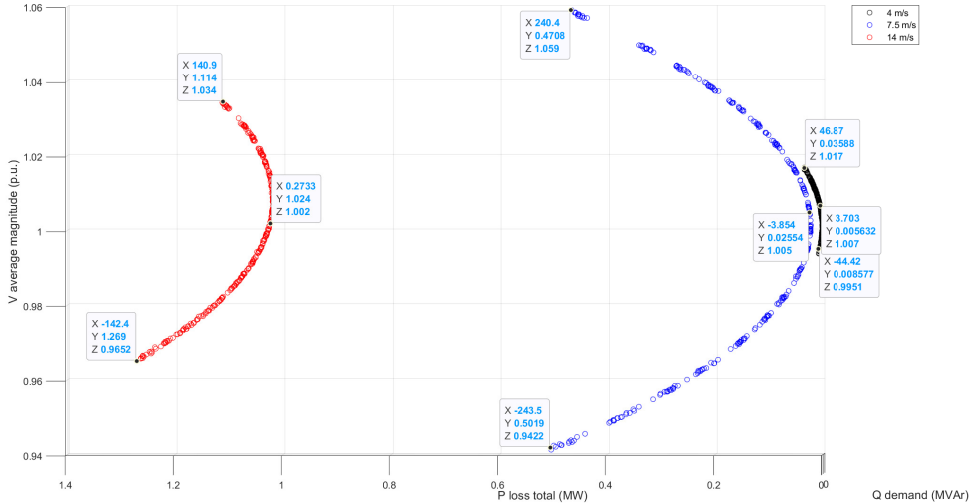


Figure 5.3: 3-D relation of the average voltage magnitude (p.u.), active power losses and random Q demands for the wind farm. The 2-D relation is shown between average voltage magnitude and Q demand.

**Reactive power demand.** In Fig. 5.3 the relation is seen between voltage and reactive power demand from the PCC. The same relation seen when analysing the 3-D relation plot for reactive power losses. This relation can be described as a positive linear dependence. Eq. 5.2 describes an exponential load model [12]. Using Eq. 5.2 with a  $k_{qu}$ , it could be derived that the relation shown in Fig. 5.3 describes a constant current load. Since further definition of this term is not part of the scope of this project, the reader is advised to study [12] for a deepened explanation about the exponential load model concept.

$$Q = Q_n \cdot (V/V_n)^{k_{qu}} \quad (5.2)$$

**Losses in the system.** Since the reactive power losses and injections in the system are relatively high compared to the active power losses, it was decided to inspect which components are responsible for this be-

haviour of the system. It can be seen from Fig. 5.4 that most losses are formed at the branches 1, 4 and 5. The equivalent branch bus indication are branches 1-2, 3-4 and 5-6. From App. 1.1, this is the branch to the PCC and the branches model for the reactance of the two main transformers. There are several reasons the highest losses are formed at these branches. Firstly, the reactance of the transformers are 0.0625 p.u., which is very high compared to other branches of the system. Secondly, these three branches deal with the highest power flows in the system, using Eq. 4.5, causing more losses. Branch will always pass the total active and reactive power generation of the system to the PCC. In conclusion, if an accurate model is desired, the effects of the transformer losses should be inspected for different test conditions.

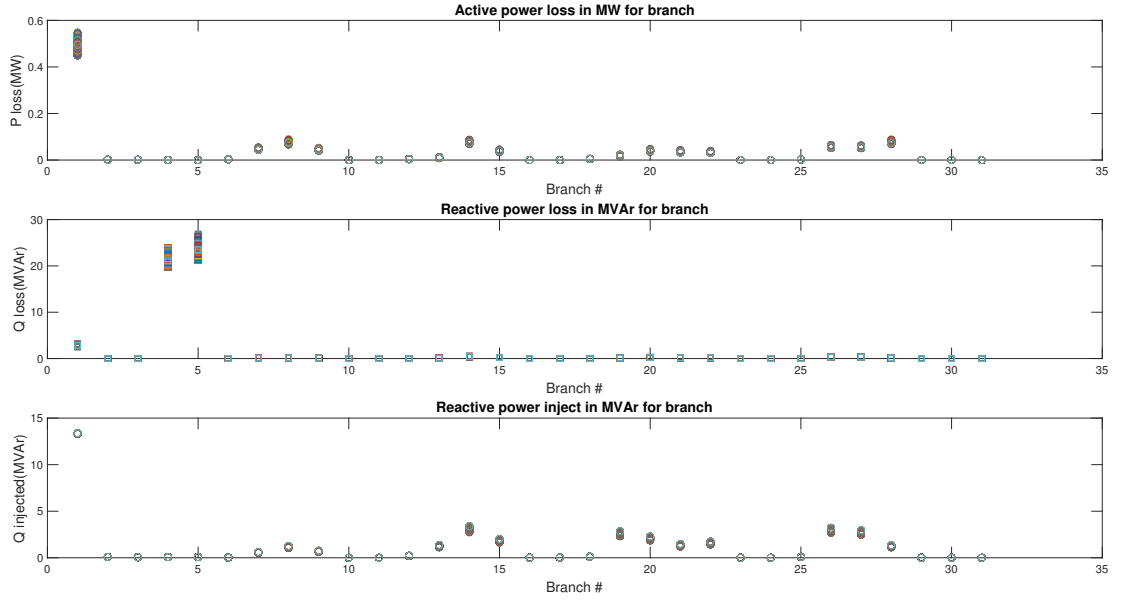


Figure 5.4: Active, reactive, injective losses in the each branch of the wind farm system with a wind speed of 14 m/s. The 2 busses connected to the specified branch are shown in App. A.2.3.

### 5.2.2. Shunt reactor on wind farm

When the shunt reactor is connected, the WTG strings will receive the same reactive power setpoints. However, an additional -12 MVar is generated by the shunt reactor and delivered to the PCC, making the reactive power delivered to the PCC more negative. Because of this negative addition of reactive power, the power factor will never be equal to 1, since the Eq. 4.4 if Q is unequal to 0 MVar at all times. A lower power factor at the PCC, indicates that the behaviour of the system will become more capacitive. Following the explanation given in Sec. 4.1, if the PCC behaves as a capacitive element, the average voltage magnitude is lowered. Furthermore, there will be an increase in reactive power losses.

The results are shown in Figs. 5.5, 5.6, 5.7. The same relations seem to be satisfied as for the wind farm with the shunt disconnected. Therefore, the hypotheses of Sec. 4.1 will not be analysed for the system configuration. Solely, a comparison will be made between the shunt (dis)connection.

With the results plotted in Figs. 5.5, 5.6, it can be concluded that the voltage is indeed lowered. Two similar Q demands are used as reference points to analyse the system behaviour for shunt disconnected and connected, namely  $sample_{con} = [-243.50.50190.9422]$  and  $sample_{discon} = [-242.50.51530.9361]$ . However, the voltage difference is so small for similar Q demands made to the two system configurations, namely  $\Delta V = 0.0056p.u.$ , that it could be considered to be negligible. The same is concluded for the active power losses behaviour to be negligible, since  $\Delta P = 0.0134MW$ .

In Fig. 5.6, the difference in reactive power losses cannot be neglected anymore. Again, two sample points are used as reference.  $sample_{con} = [-242.422.080.9425]$  and  $sample_{discon} = [-242.524.370.9361]$ .  $\Delta Q =$

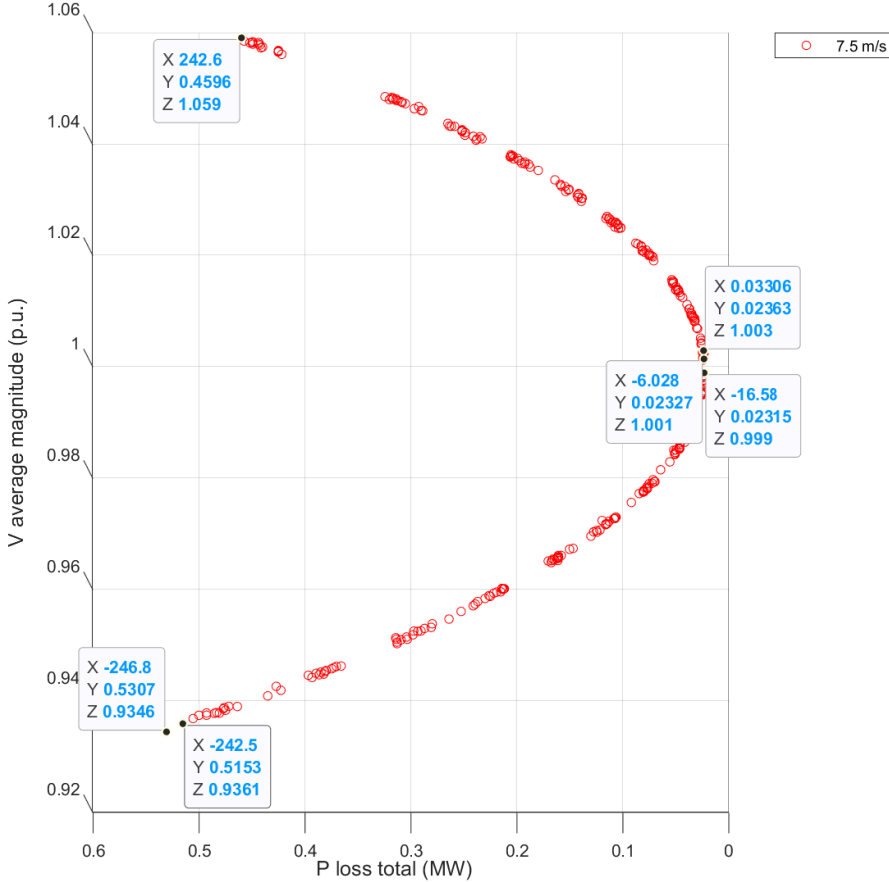


Figure 5.5: 3-D relation of the of the average voltage magnitude(p.u.), active power losses and random Q demands. Shunt reactor is connected.

2.29 MVar, making the difference caused by the shunt necessary to take into account. If this is neglected for reactive power losses, there is the possibility that the wrong optimization setpoints are calculated.

The voltage- injection relation with the shunt connected in Fig. 5.7, seems to be reasonably the same as the voltage-injection for the shunt disconnected Fig. 5.2. This was not unexpected, since initially it was thought that the droop coefficient changes for every update of the system configuration [17]. If it is analysed, what exactly makes the voltage-injection relation to change, it is the active power flow that influences this. The shunt reactor solely provides negative reactive power to the system. Hence, the active power flow is not influence, for which the linear relation is relatively the same.

### 5.2.3. Solar farm

In App. A.3.2, the data of the test models designed for the solar irradiances of Tab. 4.3, is processed and its results are plotted. The most important sample points are shown in Tab. 5.7. The data indicates that the effect the solar farm has on the system behaviour are minimal. The average voltage magnitude barely deviates from the slack node voltage of 1 p.u., which indicates the power flows are so small, that the system is considered to be stable. In addition, because of this small voltage difference, using Eqs. 4.7, 4.6, the losses are very small. The results prove this estimation to be correct. On the other hand, the results indicate that the losses are higher for voltage magnitudes above 1 p.u. While the hypotheses predicted higher losses for voltage magnitudes below 1 p.u. The explanation for this, is that although this is contrary to the expected, the losses are of such magnitude, that the difference is negligible. Because of this small difference, the results are not sufficient to disprove the hypotheses. Furthermore, the hypotheses are satisfied for the wind farm and hybrid farm, which cause more fluctuations in the system behaviour for different generations.

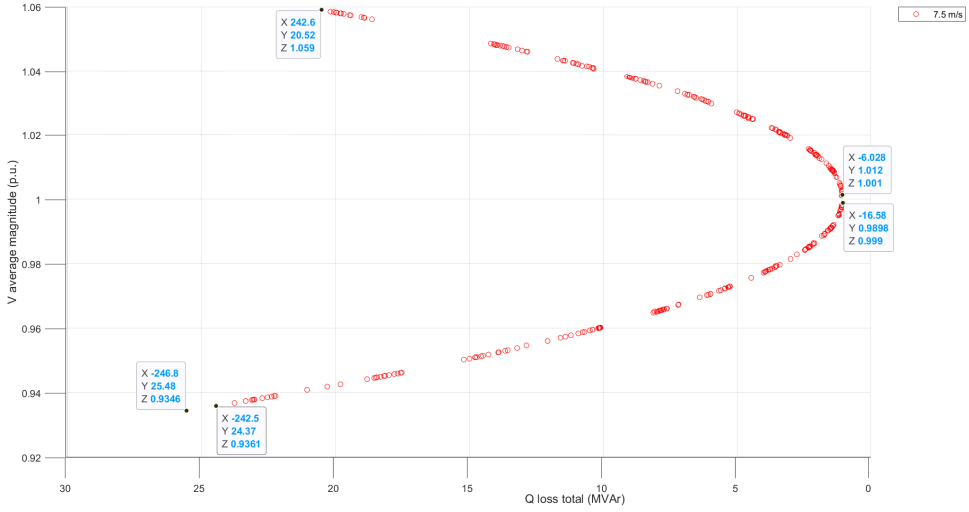


Figure 5.6: 3-D relation of the of the average voltage magnitude(p.u.), reactive power losses and random Q demands. Shunt reactor is connected.

The relations for losses and injections explained in Sec. 4.1 are satisfied. In conclusion, the system behaviour is very stable with the implementation of the solar farm. Therefore, the solar farm can be combined with the wind farm, without a negative effect on the system behaviour. The expectation is that the hybrid farm will not lead to violation of system constraints if the wind farm did not cause this behaviour already. This discussion is elaborated in Subsec. 5.2.4.

Table 5.7: Results for the maximum and minimum average voltage magnitude for the solar farm in App. A.3.2.

	Voltage max(p.u.)	P loss (MW)	Q loss (MVAr)	Q inj (MVAr)	Voltage min (p.u.)	P loss (MW)	Q loss (MVAr)	Q inj (MVAr)
Irr 100 W/m2	1.001	0.002102	0.05042	19.46	1	0.0009225	0.01844	19.43
Irr 500 W/m2	1.002	0.01903	0.4438	19.49	0.9995	0.01575	0.3508	19.4
Irr 800 W/m2	1.003	0.045	1.044	19.52	0.9987	0.4098	0.9209	19.37

### 5.2.4. Hybrid farm

**Active and reactive power losses.** The test models were run for the hybrid farm in the same way as they were run for the wind farm as described in Sec. 4.2. It was expected that for the hybrid farm the same 3-D will be visible as shown and elaborated for the wind farm, described in Subsec. 5.2.1. However, the active power generation in each o.c. will be higher for the hybrid farm, since additional power is generated by the photovoltaic strings. Fig. 5.8 visualizes indeed the same relation as shown in Fig. 5.1 for the wind farm. However, as illustrated by Tab. 5.8, there is a significant difference in the amount of losses. Since the power generation for the hybrid farm is higher than that of the wind farm, both the active and reactive power losses will be higher. The exact numbers are shown in Tab.5.8. Furthermore, Fig. 5.1 and Tab. 5.8 show that the higher the generation, the difference between the losses of each farm. These results are in line with the hypotheses made in Sec. 4.1.

Table 5.8: Comparison of Wind and Hybrid farm losses

Operating condition	$P_{lossmax}$ Wind [MW]	$P_{lossmax}$ Hybrid [MW]	$Q_{lossmax}$ Wind [MVAr]	$Q_{lossmax}$ Hybrid [MVAr]
Low generation (4 m/s)	0.03588	0.04188	1.775	2.207
Nominal generation (7.5 m/s)	0.5019	0.5266	22.69	25.72
High generation (14 m/s)	1.269	1.481	56.84	72.5

**Reactive power injections** For the reactive power injections, it was expected that the same linear relation will hold as shown in Fig.5.2 for the wind farm and as explained in Eq. 4.8. As shown in Fig.5.9, this linear

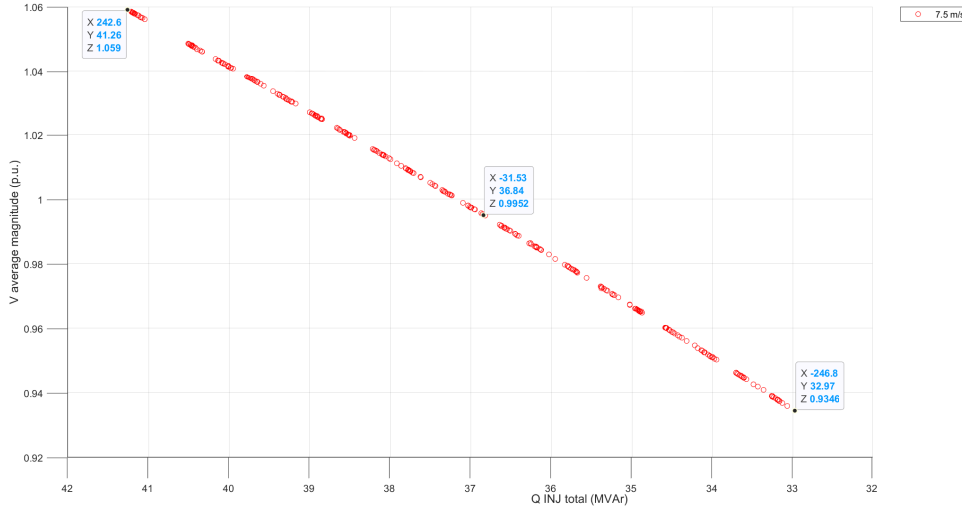


Figure 5.7: 3-D relation of the of the average voltage magnitude(p.u.), injection power losses and random Q demands. Shunt reactor is connected.

relation also holds for the hybrid farm. However, the maximum injected reactive power for the hybrid farm is significantly higher than that of the wind farm as shown in Tab. 5.9. This is in line with Eq. 4.8, since a higher average voltage magnitude in the hybrid farm results in a larger maximum injected reactive power. The linear line shown in Fig.5.2 is extended in Fig. 5.9.

Table 5.9: Maximum Reactive power injections for the wind and hybrid farm.

Farm	Maximum reactive power injection [MVAr]
Wind farm	41.45
Hybrid farm	47.97

### 5.2.5. String level

### 5.3. Prototype

The prototype will consist of two snapshots in which the power flow is indicated for all branches of the system.

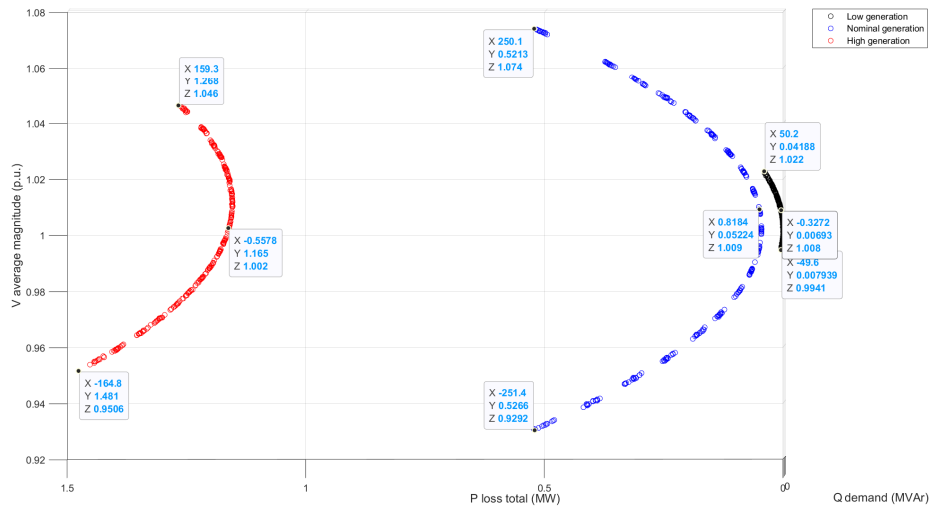


Figure 5.8: 3-D relation of the of the average voltage magnitude(p.u.), active power losses and random Q demands for the hybrid farm.

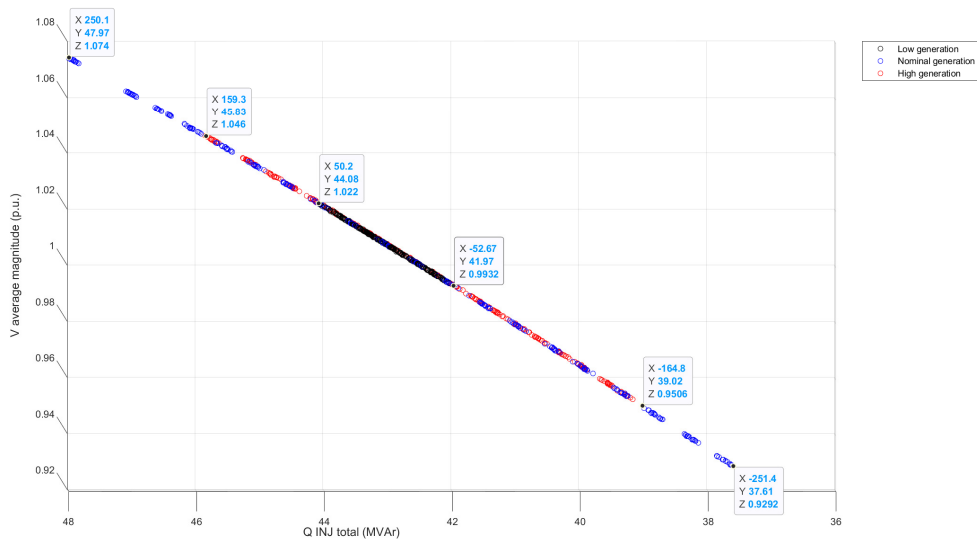


Figure 5.9: 3-D relation of the of the average voltage magnitude(p.u.), injection power losses and random Q demands for the hybrid farm.

# 6

## Conclusion

### 6.1. Conclusion

The same relations seem to be held not only for different system configuration, i.e. wind farm, solar farm and hybrid farm, but also for different dispatches leading to a variation in apparent power generation. This is desired, since it means that the system behaviour could be predicted for a variation in operating conditions.

From the results in Chap. 5, it can be concluded that the system is relatively stable. This makes the future expansion of the system configuration with additional PV or WTG strings feasible. There is no violations of the system constraints, i.e. cable ratings or voltage limits to the input of the transformer.

### 6.2. Recommendations

For future research, it is recommended to inspect the losses caused by the transformer. Furthermore, it is recommended to use a 3-winding transformer model rather than a 2-winding transformer to improve the accuracy for a realistic system behaviour. The reason the accuracy is improved by this, is because the transformer are responsible for the limitations in the system for voltage and power flow, making it the weakest component to take into consideration when modeling a similar transmission system.

# Bibliography

- [1] ABB. Abb central inverters. [https://library.e.abb.com/public/4736ece73ecf4e3aa2bb7a6ec7f0ee6d/PVS800\\_central\\_inverters\\_flyer\\_3AUA0000057380\\_RevN\\_EN\\_lowres.pdf](https://library.e.abb.com/public/4736ece73ecf4e3aa2bb7a6ec7f0ee6d/PVS800_central_inverters_flyer_3AUA0000057380_RevN_EN_lowres.pdf), 2017. Accessed on 2020-05-21.
- [2] A.Y. Abdelaziz, Mahmoud M. Othman, M. Ezzat, and A.M. Mahmoud. A novel monte carlo based modeling strategy for wind based renewable energy sources. *Eighteenth International Middle East Power Systems Conference (MEPCON)*, December 2016. DOI: 10.1109/MEPCON.2016.7836897.
- [3] European Environment Agency. Making clean renewable energy happen. <https://www.eea.europa.eu/signals/signals-2017/articles/making-clean-renewable-energy-happen>, November 2017. Accessed on 2020-05-10.
- [4] S. Conti and S. Raiti. Probabilistic load flow for distribution networks with photovoltaic generators part 1: Theoretical concepts and models. *International Conference on Clean Electrical Power*, May 2007. DOI: 10.1109/ICCEP.2007.384199.
- [5] Tu Delft. Dutch pv portal. <https://www.tudelft.nl/en/eemcs/the-faculty/departments/electrical-sustainable-energy/photovoltaic-materials-and-devices/dutch-pv-portal/>, 2020. Accessed on 2020-05-05.
- [6] K.C. Divya and P.S. Nagendra Rao. Models for wind turbine generating systems and their application in load flow studies. *Electric Power Systems Research*, 76:844–856, June 2006. DOI: 10.1016/j.epsr.2005.10.012.
- [7] ESIG. Reactive power capability and interconnection requirements for pv and wind plants. <https://www.esig.energy/wiki-main-page/reactive-power-capability-and-interconnection-requirements-for-pv-and-wind-plants/>, 2020. Accessed on 2020-05-05.
- [8] A. Etxegarai, P. Eguia, E. Torres, G. Buigues, and A. Iturregi. Current procedures and practices on grid code compliance verification of renewable power generation. *Renewable and sustainable energy reviews*, February 2015.
- [9] A. Etxegarai, P. Eguia, E. Torres, G. Buigues, and A. Iturregi. Incorporation of probabilistic solar irradiance and normally distributed load for the assessment of atc. *8th International Conference on Computing, Communication and Networking Technologies (ICCCNT)*, July 2017.
- [10] Andres E. Feijoo and Jose Cidras. Modeling and analysis of wind farms in the load flow analysis. *IEEE Transactions on Power Systems*, 15(1), February 2000. DOI:10.1109/ICCP-EIC.2015.7259482.
- [11] A.F. Glimm and G.W. Stagg. Automatic calculation of load flows. *AIEEE Transaction on Power Apparatus and Systems*, 76:817–828, October 1957.
- [12] Working group C4.605. *Modelling and aggregation of loads in flexible power networks*. 2014.
- [13] K.E. Hagan and O.O. Oyebajo. A probabilistic forecasting model for accurate estimation of pv solar and wind power generation. *IEEE Power and Energy Conference at Illinois (PECI)*, February 2016.
- [14] I.Munteanu. *Optimal control of wind energy systems: towards a global approach*.
- [15] SRA International. Solar power analysis and design specifications. 2017. Accessed on 2020-05-10.
- [16] K.N. VWHV-UO-3.2.OS-OWN-E0014032-E01-FA0-000001-E-overall Single Line. ABB Power Grids The Netherlands B.V., 2020. Approved by Gregory Kinburn ABB PGGI Rotterdam.

- [17] Y. Li, Z. Xu, J. Zhang, and K. Meng. Variable droop voltage control for wind farm. *IEEE Transactions on Sustainable Energy*, 9(1), January 2018.
- [18] F.H. Mahmood, A.K. Resen, and A.B. Khamees. Wind characteristic analysis based on weibull distribution of al-salman site, iraq. *Energy reports*, February 2020.
- [19] P. Mayer. Steady-state grid compliance report. July 2019.
- [20] P. Priyadarshini and M. Mohamed Thameem Ansari. Modeling and analysis of wind farms in load flow studies. *International Conference on Computation of Power, Energy, Information and Communication (ICCPEIC)*, April 2015. DOI: 10.1109/ICCPEIC.2015.7259482.
- [21] R. Ramakrishna, A. Scaglione, V. Vittal, E. Dall'Anese, and A. Bernstein. A model for joint probabilistic forecast of solar photovoltaic power and outdoor temperature. *IEEE Transactions on Signal Processing*, 67(24), November 2019.
- [22] Sunpower. Sunpower x-series. <https://us.sunpower.com/sites/default/files/media-library/data-sheets/sunpower-x-series-residential-solar-panels-x22-360-datasheet-514618-rev0.pdf>, September 2017. Accessed on 2020-05-05.
- [23] W.F. Tinney and C.E. Hart. Power flow solution by newton's method. *IEEE Transaction on Power Apparatus and Systems*, PAS-86(11):1449–1460, November 1967.
- [24] A. Cabrera Tobar, E. Bullich-Massague, M. Arruages-Penalba, and O. Gomis-Bellmunt. Reactive power capability analysis of a photovoltaic generator for large scale power plants. *5th IET International Conference on Renewable Power Generation (RPG)*, 2016. DOI: 10.1049/cp.2016.0574.
- [25] S.L. Walker. Building mounted wind turbines and their suitability for the urban scale—a review of methods of estimating urban wind resource. *Energy and buildings*, August 2011.
- [26] L. Webb. How has the renewable energy market changed in the last decade? <https://www.nesgt.com/blog/2020/01/how-has-the-renewable-energy-market-changed-in-the-last-decade>, January 2020. Accessed on 2020-05-01.
- [27] Z-S. Zhang, Y-Z. Sun, J. Lin, L. Cheng, and G-J. Li. Versatile distribution of wind power output for a given forecast value. *IEEE Power and Energy Society General Meeting*, July 2012.
- [28] R. D. Zimmerman and C.E. Murillo-Sánchez. Matpower user's manual. 2019.
- [29] N.A. Zulkilfi, N.M.M. Razali, M. Marsadek, and A.K. Ramasamy. Probabilistic analysis of solar photovoltaic output based on historical data. *IEEE 8th International Power Engineering and Optimization Conference (PEOCO2014)*, March 2014.

# A

## Appendix

### A.1. Additional overviews

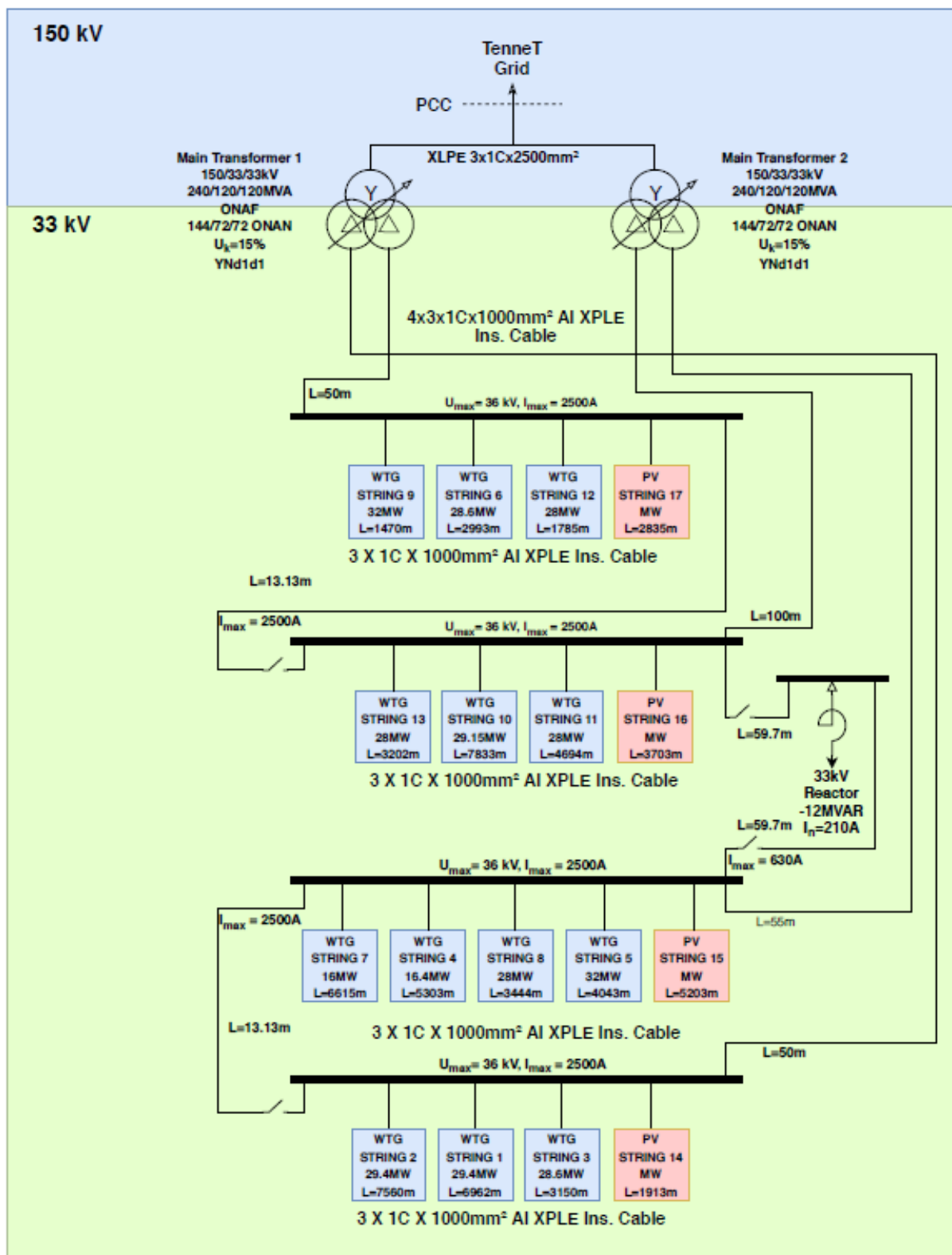


Figure A.1: Schematic of case system

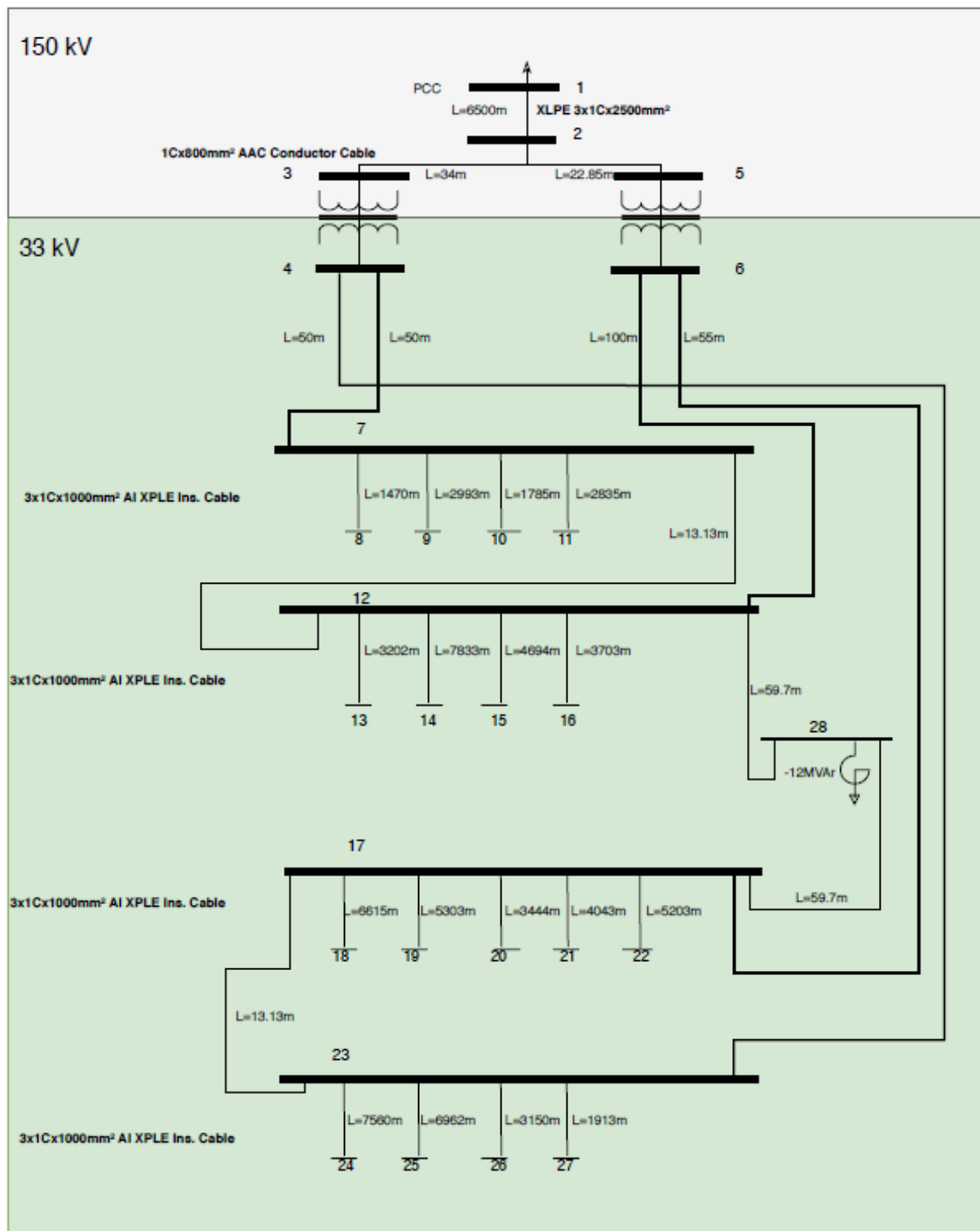


Figure A.2: Overview of case system used in MatPower

String	Index	Address	Enercon Type	WPZ Type	P_nom [kW]	P_string [MW]
Bus 25	1	A27-01	E-138	A	4200	29.4
	2	A27-02	E-138	A	4200	
	3	A27-03	E-138	A	4200	
	4	A27-04	E-138	A	4200	
	5	A27-05	E-138	A	4200	
	6	A27-06	E-138	A	4200	
	7	A27-07	E-138	A	4200	
Bus 24	8	A27-11	E-138	A	4200	29.4
	9	A27-12	E-138	A	4200	
	10	A27-13	E-138	A	4200	
	11	A27-14	E-138	A	4200	
	12	A27-15	E-138	A	4200	
	13	A27-16	E-138	A	4200	
	14	A27-17	E-138	A	4200	
Bus 26	15	A27-08	E-138	A	4200	29.4
	16	A27-09	E-138	A	4200	
	17	A27-10	E-138	A	4200	
	18	ADW-05	E-115	C	4200	
	19	ADW-06	E-115	C	4200	
	20	ADW-07	E-115	C	4200	
	21	ADW-08	E-115	C	4200	
Bus 19	22	ADW-01	E-138	A	4200	16.8
	23	ADW-02	E-138	A	4200	
	24	ADW-03	E-115	C	4200	
	25	ADW-04	E-115	C	4200	
Bus 21	26	ADW-11	E-126	B	4000	32
	27	ADW-12	E-126	B	4000	
	28	ADW-13	E-126	B	4000	
	29	ADW-14	E-126	B	4000	
	30	ADW-15	E-126	B	4000	
	31	ADW-16	E-126	B	4000	
	32	ADW-17	E-126	B	4000	
Bus 9	33	ADW-18	E-126	B	4000	29.4
	34	ADO-01	E-138	A	4200	
	35	ADO-02	E-138	A	4200	
	36	ADO-03	E-138	A	4200	
	37	ADO-04	E-115	C	4200	
	38	ADO-05	E-115	C	4200	
	39	ADO-06	E-115	C	4200	
Bus 18	40	ADO-07	E-115	C	4200	16
	41	ADW-19	E-126	B	4000	
	42	ADW-20	E-126	B	4000	
	43	ADO-20	E-126	B	4000	
	44	ADO-22	E-126	B	4000	

Figure A.3: Overview of different Enercon WTG types connected to each string of the transmission system [19] [16].

	45	ADO-14	E-126	B	4000	
	46	ADO-15	E-126	B	4000	
	47	ADO-16	E-126	B	4000	
Bus 20	48	ADO-17	E-126	B	4000	28
	49	ADO-18	E-126	B	4000	
	50	ADO-19	E-126	B	4000	
	51	ADO-21	E-126	B	4000	
	52	ADO-08	E-115	C	4200	
	53	ADO-09	E-115	C	4200	
Bus 8	54	ADO-10	E-115	C	4200	33
	55	ADO-11	E-126	B	4000	
	56	ADO-12	E-126	B	4000	
	57	ADO-13	E-126	B	4000	
	58	ADW-09	E-115	C	4200	
	59	ADW-10	E-115	C	4200	
	60	SCH-01	E-103	D	2350	
	61	SCH-02	E-103	D	2350	
	62	SCH-03	E-103	D	2350	
Bus 14	63	SCH-04	E-103	D	2350	29.15
	64	SCH-05	E-103	D	2350	
	65	SCH-06	E-103	D	2350	
	66	SCH-07	E-103	D	2350	
	67	SCH-08	E-103	D	2350	
	68	SCH-09	E-103	D	2350	
	69	LPT-11	E-126	B	4000	
	70	LPT-12	E-126	B	4000	
	71	LPT-04	E-126	B	4000	
Bus 15	72	LPT-05	E-126	B	4000	28
	73	LPT-06	E-126	B	4000	
	74	LPT-07	E-126	B	4000	
	75	LPT-08	E-126	B	4000	
	76	LPT-09	E-126	B	4000	
	77	LPT-10	E-126	B	4000	
	78	LPT-03	E-126	B	4000	
	79	RDT-08	E-115	C	4200	
Bus 10	80	RDT-09	E-115	C	4200	28.8
	81	RDT-10	E-115	C	4200	
	82	RDT-11	E-126	B	4000	
	83	RDT-12	E-126	B	4000	
	84	RDT-13	E-115	C	4200	
	85	RDT-01	E-126	B	4000	
Bus 13	86	RDT-02	E-126	B	4000	28.8
	87	RDT-03	E-126	B	4000	
	88	RDT-04	E-115	C	4200	
	89	RDT-05	E-115	C	4200	
	90	RDT-06	E-115	C	4200	
	91	RDT-07	E-115	C	4200	
				Total		
				358.15	358.15	

Figure A.4: Overview of different Enercon WTG types connected to each string of the transmission system [19] [16].

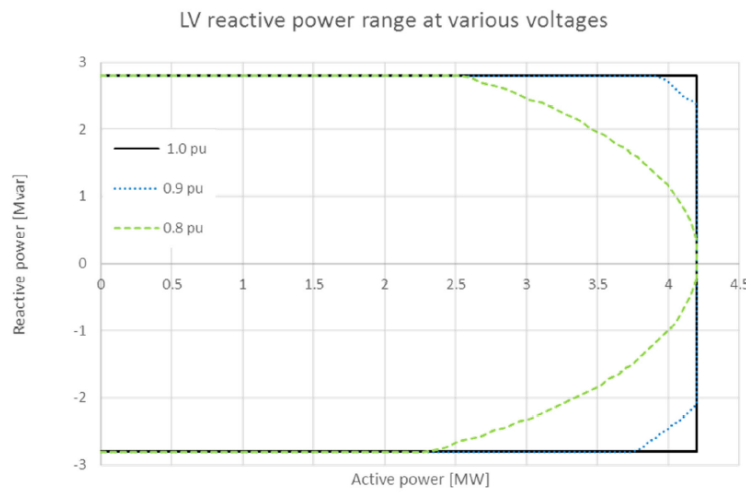


Figure A.5: Common case for relation between P and Q of WTG

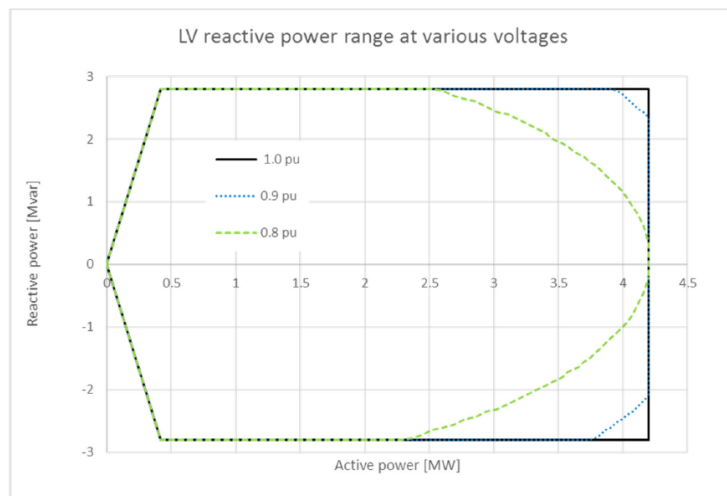


Figure A.6: Non-ideal case for relation between P and Q of WTG

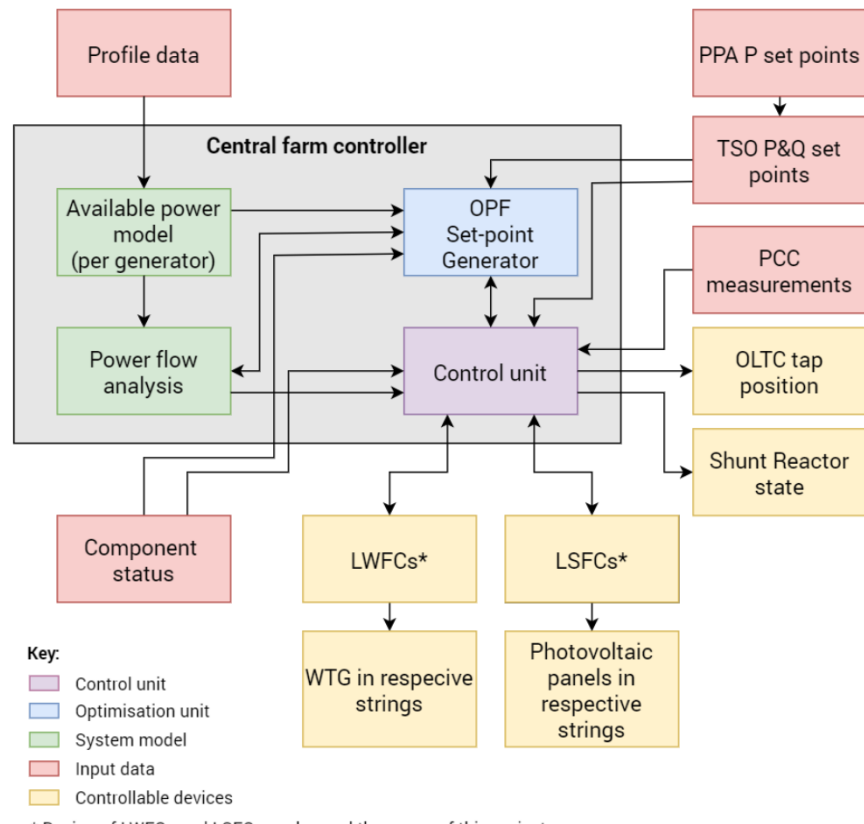


Figure A.7: Overview of interaction between the three components that together form the optimisation unit.

### A.1.1. Group interaction

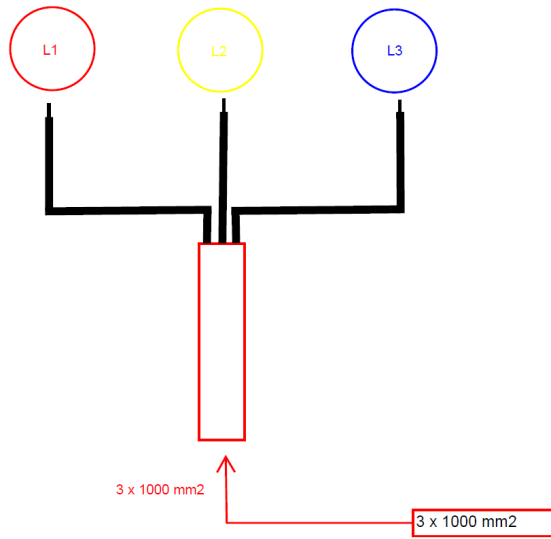


Figure A.8: Cable configuration for a  $3 \times 1000\text{ mm}^2$  XLPE Al cable. Data from [19].

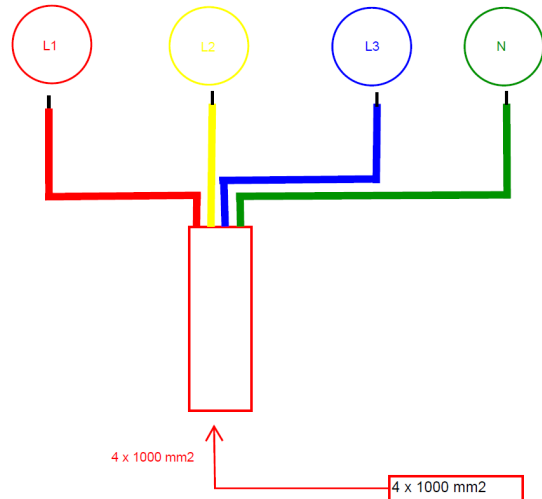


Figure A.9: Cable configuration for a  $4 \times 1000\text{ mm}^2$  XLPE Al cable. Data from [19].

## A.2. Cable modeling

### A.2.1. Cable configurations

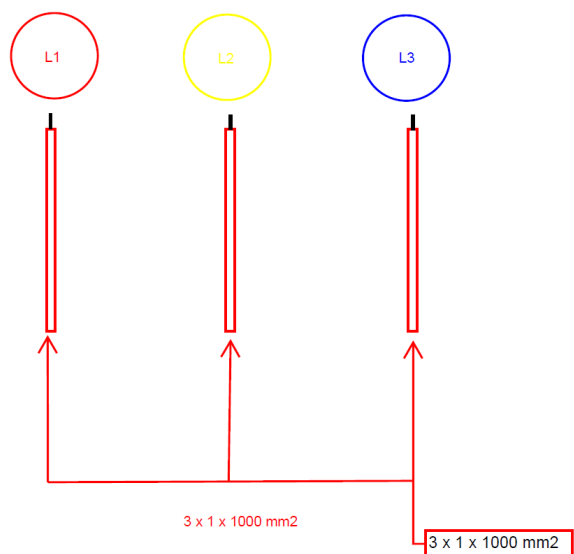


Figure A.10: Cable configuration for a  $3 \times 1 \times 1000\text{mm}^2$  XLPE Al cable. Data from [19].

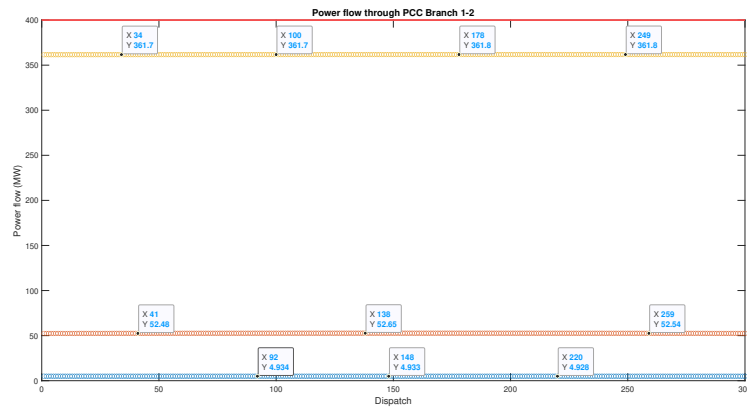


Figure A.11

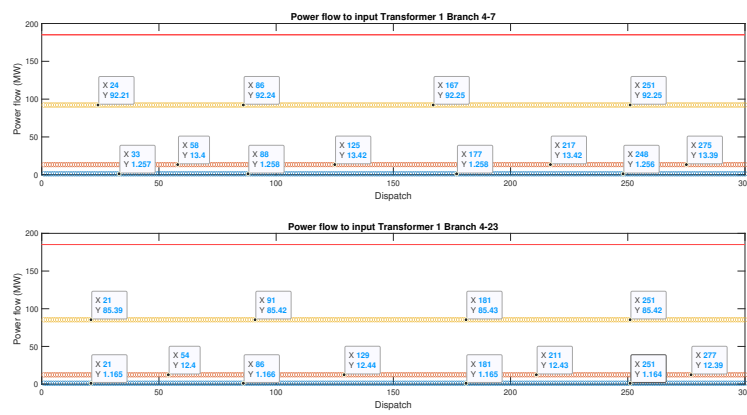


Figure A.12

## A.2.2. Branch calculations

## A.2.3. Branch connections to bus

## A.3. Results

### A.3.1. Wind farm Plots

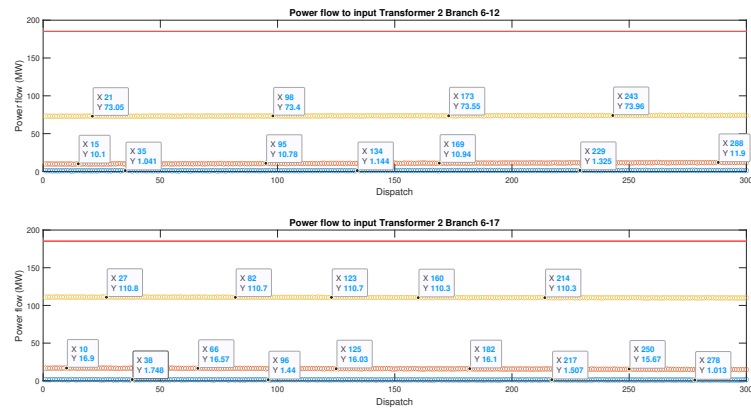


Figure A.13

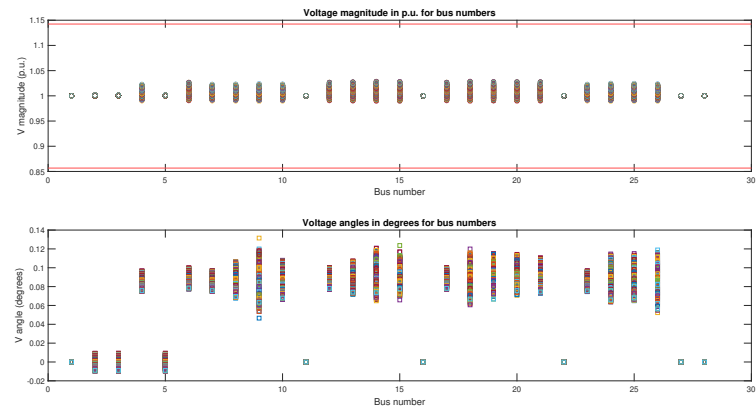


Figure A.14

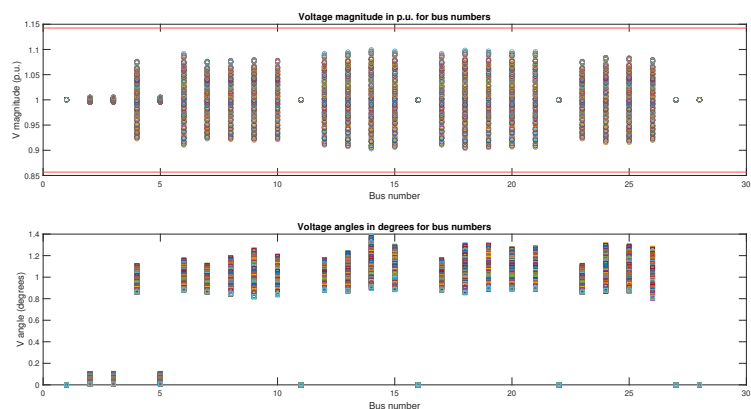


Figure A.15

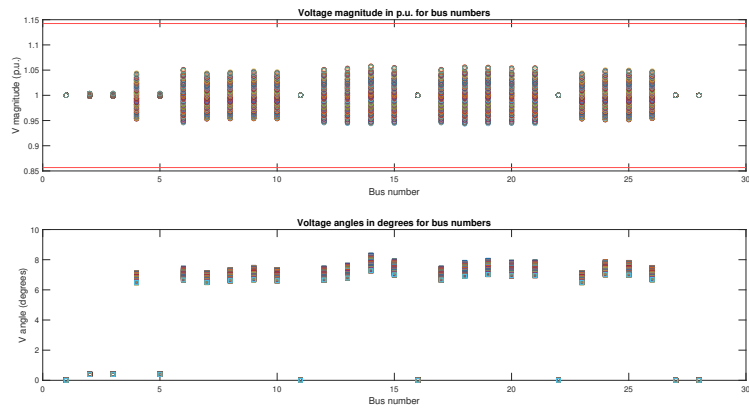


Figure A.16

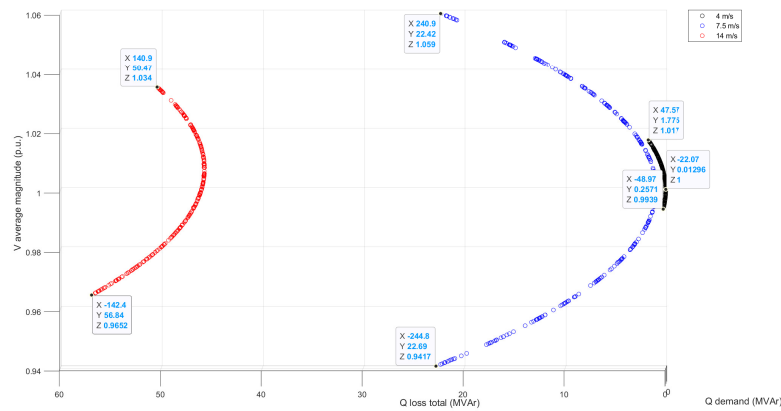


Figure A.17

### A.3.2. Solar farm Plots

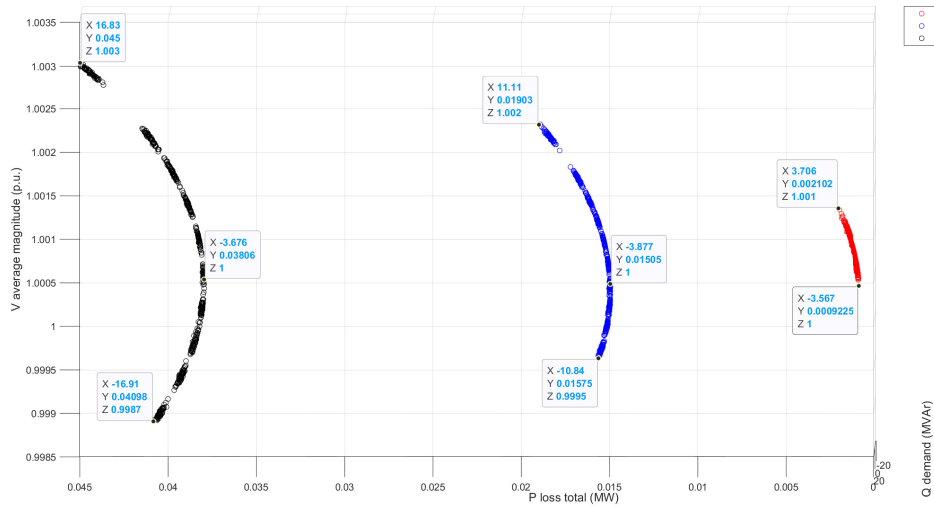


Figure A.18: 3-D relation plot of active power losses for the solar farm.

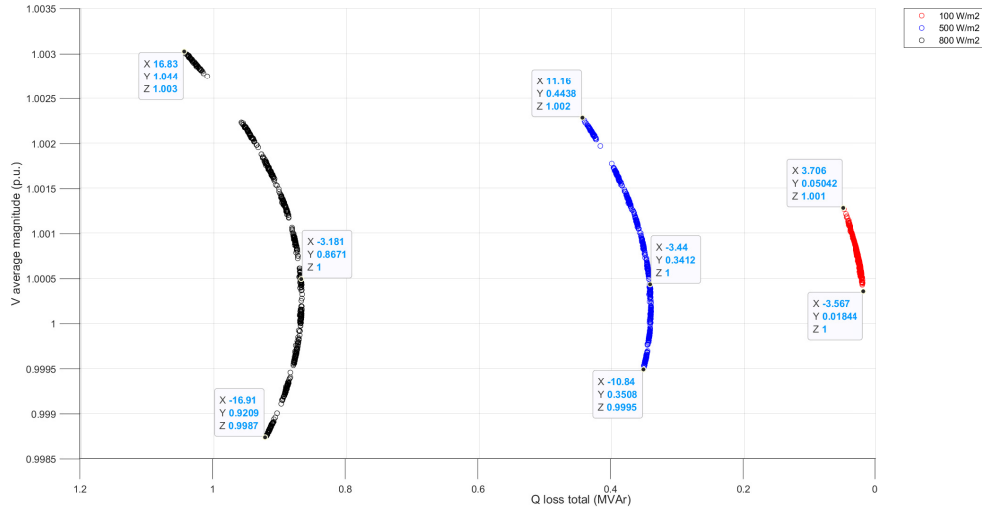


Figure A.19: 3-D relation plot of reactive power losses for the solar farm.

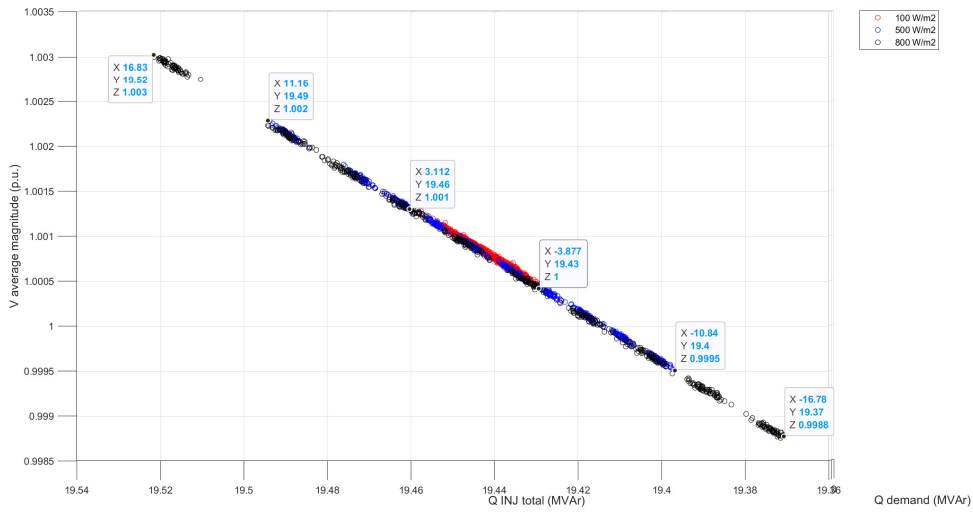


Figure A.20: 3-D relation plot of reactive power injection for the solar farm.

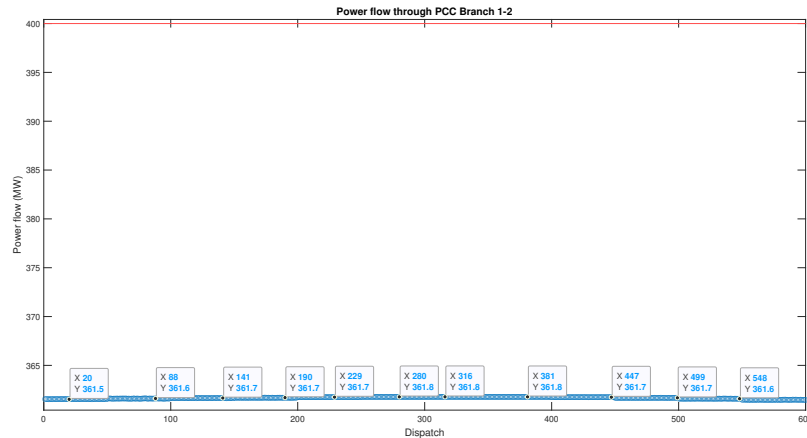


Figure A.21: Caption

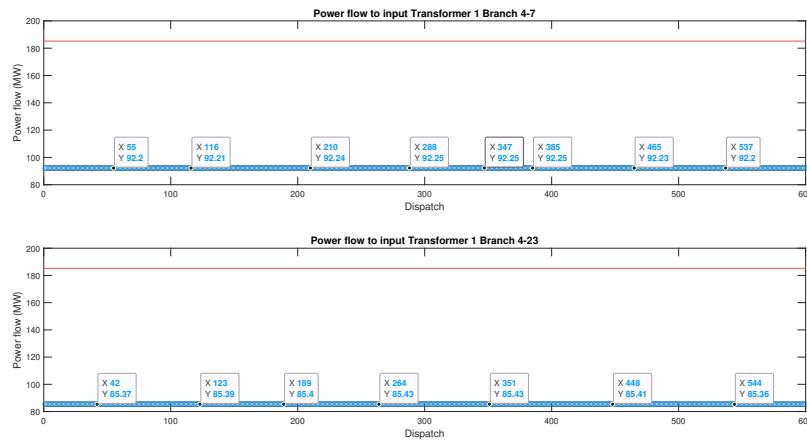


Figure A.22: Power flow through branch 4-7 and 4-23 for the solar farm. From down to up, solar irradiance = 100;500;800 W/m².

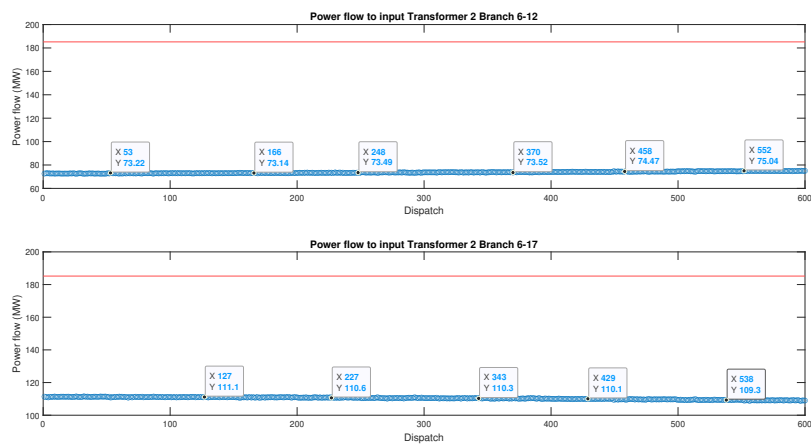


Figure A.23: Power flow through branch 6-12 and 6-17 for the solar farm. From down to up, solar irradiance = 100;500;800 W/m<sup>2</sup>.

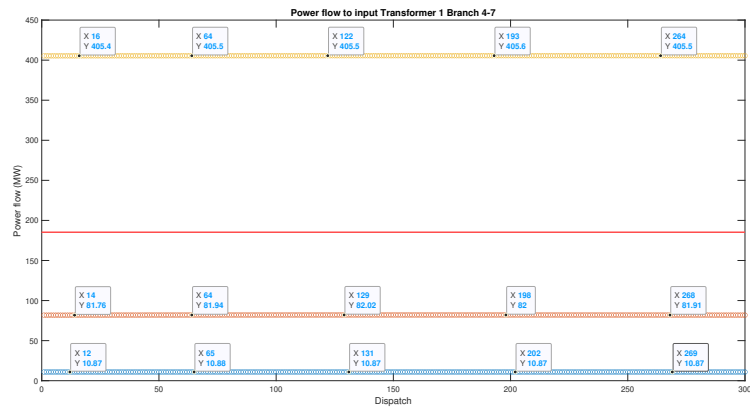


Figure A.24

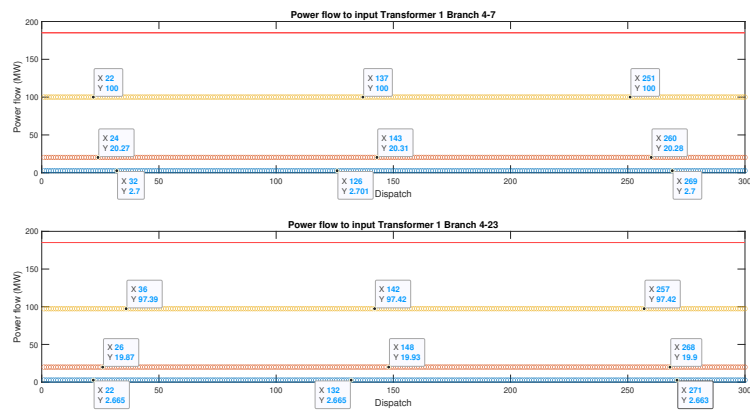


Figure A.25

### A.3.3. Hybrid farm Plots

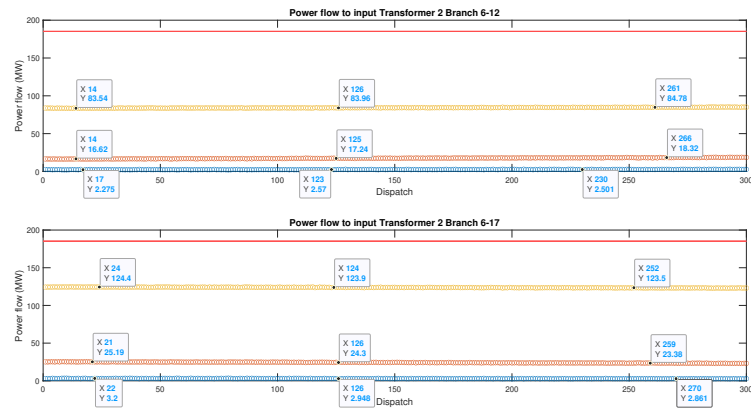


Figure A.26

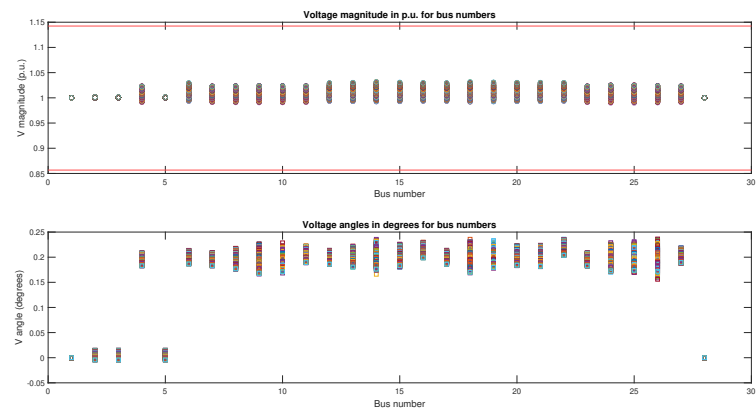


Figure A.27

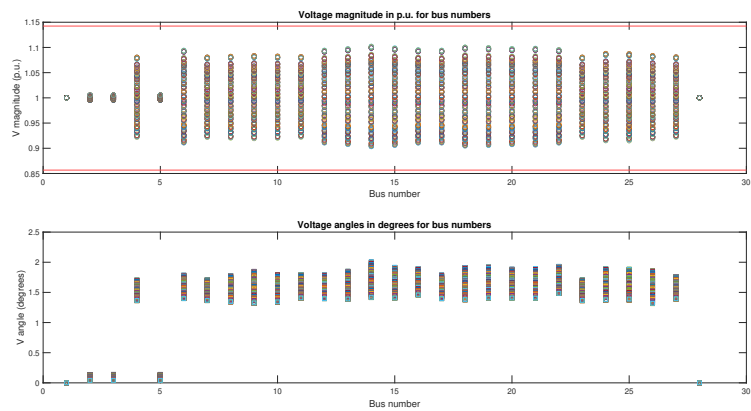


Figure A.28

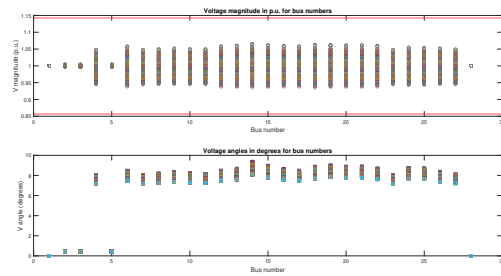


Figure A.29

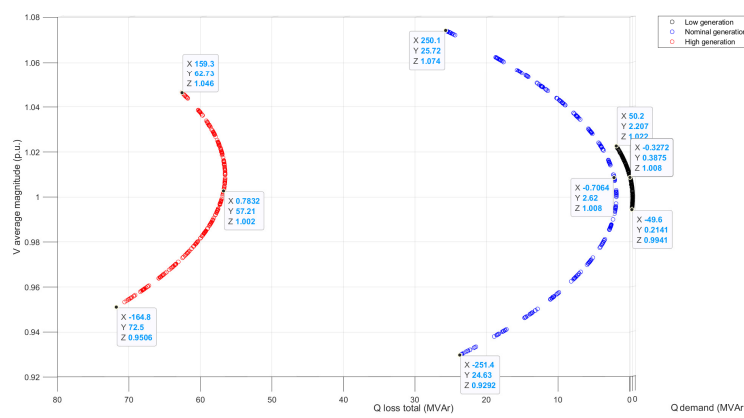


Figure A.30

## A.4. MatLab codes

### A.4.1. Newton Raphson method

```

%%Authors: F. Rimon and M. Mastouri
%Last edited: 05/06/2020

%This is a method that simulates the hand calculations done to solve a
%Newton Raphson Power flow

%The case study used is a branch of the case study of the Bachelor
%Thesis
%Project of Group 09.01
close all;
clear all;
clc
%% Power flow for Node 1(Bus 24) of Branch 23-24 with Q from samples_Q
% data #Dispatch 1000
% %Workspace needs to be included

done = 0;
iter = 1; %count iterations needed
while(done == 0 )

mag = 1;
angle = 0;
P_1 = 0.294;
Q_1 = 0.0169;

P1 = (mag*7.1621*cosd(angle-118.6)+7.326*cosd(-80)*(mag^2));
Q1 = (mag*7.1621*sind(angle-118.6)-7.326*sind(-80)*(mag^2));

Calculate derivatives
diff_P1_angle = -7.1621*mag*sind(angle-118.6);
diff_P1_mag = 7.1621*cosd(angle-118.6)+7.326*cosd(-80)*2*mag;

diff_Q1_angle = 7.1621*mag*cosd(angle-118.6);
diff_Q1_mag = 7.1621*sind(angle-118.6)-7.326*sind(-80)*2*mag;

equation to be solved
new_P = P_1-P1;
new_Q = Q_1-Q1;
delta_flow = [new_P;new_Q];

Put derivatives in Jacobian
jacob = [diff_P1_angle diff_P1_mag; diff_Q1_angle diff_Q1_mag];

Solve linear equation
x = linsolve(jacob,delta_flow);
delta_angle_degree = (x(1,:)/(2*pi))*360; %convert radian angle to
degree angle

specify new angle and magnitude
new_angle = angle - delta_angle_degree;
new_mag = mag - x(2,:);

```

```

determine if result is below threshold

if(new_P <= 0.1)
    done = 1;
    iter = iter;

else
    done = 0;
    mag = new_mag;
    angle = new_angle;
    iter = iter + 1;
end
end

%After the final answers are determined, insert them manually into
%these
%equations to determine the losses in the system.
new_angle = 19.4;
new_mag = 1.0;
Z_1 = 0.02356859504 + 0.134446281*i;
new_mag_phasor = new_mag*(cosd(new_angle)+sind(new_angle)*i);
old_mag_phasor = 0.9776*(cosd(18.5814)+sind(18.5814)*i);
I_23_24 = (new_mag_phasor - old_mag_phasor)/Z_1;
P_loss = (abs(I_23_24))^2*real(Z_1);
Q_loss = (abs(I_23_24))^2*imag(Z_1);

Base = 100;

P_loss_real = P_loss *Base;
Q_loss_real = Q_loss *Base;
%% Power flow for Node 2 (Bus 23) of Branch 23-24 with Q from samples_Q
    data #Dispatch 1000
%Workspace needs to be included
%
% done_2 = 0;
% iter_2 = 1; %count iterations needed
% while(done_2 == 0 )
%
% mag = 1;
% angle = 18;
% P_2 = -0.294;
% Q_2 = -0.0169;
% % solution = nr_method(0.9776,18.5814,0.294,0.000169)
%
% P2 = (mag*7.18*cosd(angle-119.25)+7.326*cosd(-80)*(mag^2));
% Q2 = (mag*7.18*sind(angle-119.25)-7.326*sind(-80)*(mag^2));
%
% %Calculate derivatives
% diff_P2_angle = -7.18*mag*sind(angle-119.25);
% diff_P2_mag = 7.18*cosd(angle-119.25)+7.326*cosd(-80)*2*mag;
%
% diff_Q2_angle = 7.18*mag*cosd(angle-119.25);
% diff_Q2_mag = 7.18*sind(angle-119.25)-7.326*sind(-80)*2*mag;
%
% %equation to be solved
% new_P_2 = P_2-P2;

```

```
% new_Q_2 = Q_2-Q2;
% delta_flow = [new_P_2;new_Q_2];
%
% %Put derivatives in Jacobian
% jacob = [diff_P2_angle diff_P2_mag; diff_Q2_angle diff_Q2_mag];
%
% %Solve linear equation
% x = linsolve(jacob,delta_flow);
% delta_angle_degree = (x(1,:)/(2*pi))*360; %convert radian angle to
degree angle
%
% %specify new angle and magnitude
% new_angle = angle - delta_angle_degree;
% new_mag = mag - x(2,:);
%
% %determine if result is below threshold
%
% if(new_P_2 <= 0.00001)
%     done_2 = 1;
%     iter_2 = iter_2;
%
% else
%     done_2 = 0;
%     mag = new_mag;
%     angle = new_angle;
%     iter_2 = iter_2 + 1;
% end
% end
%% Power flow for Node 2 of Branch 23-24 with Q from generator pf data
#Dispatch 1000
% % %Workspace needs to be included
%
% % done = 0;
% % iter = 1; %count iterations needed
% % while(done == 0 )
% %
% % mag = 1.01;
% % angle = 20.7;
% % P_1 = 0.294;
% % Q_1 = 0.000256;
% %
% % P1 =(mag*7.1621*cosd(angle-118.6)+7.326*cosd(-80)*(mag^2));
% % Q1 = (mag*7.1621*sind(angle-118.6)-7.326*sind(-80)*(mag^2));
% %
% % Calculate derivatives
% % diff_P1_angle = -7.1621*mag*sind(angle-118.6);
% % diff_P1_mag = 7.1621*cosd(angle-118.6)+7.326*cosd(-80)*2*mag;
% %
% % diff_Q1_angle = 7.1621*mag*cosd(angle-118.6);
% % diff_Q1_mag = 7.1621*sind(angle-118.6)-7.326*sind(-80)*2*mag;
% %
% % equation to be solved
% % new_P = P_1-P1;
% % new_Q = Q_1-Q1;
% % delta_flow = [new_P;new_Q];
% %
```

```
% % Put derivatives in Jacobian
% % jacob = [diff_P1_angle diff_P1_mag; diff_Q1_angle diff_Q1_mag];
% %
% % Solve linear equation
% % x = linsolve(jacob,delta_flow);
% % delta_angle_degree = (x(1,:)/(2*pi))*360; %convert radian angle to
% degree angle
% %
% % specify new angle and magnitude
% % new_angle = angle - delta_angle_degree;
% % new_mag = mag - x(2,:);
% %
% % determine if result is below threshold
% %
% % if(new_P <= 0.001)
% %     done = 1;
% %     iter = iter;
% %
% % else
% %     done = 0;
% %     mag = new_mag;
% %     angle = new_angle;
% %     iter = iter + 1;
% % end
% % end

% new_angle = 19.7;
% new_mag = 0.9801;
% Z_1 = 0.02356859504 + 0.134446281*i;
% new_mag_phasor = new_mag*(cosd(new_angle)+sind(new_angle)*i);
% old_mag_phasor = 0.9776*(cosd(18.5814)+sind(18.5814)*i);
% I_23_24 = (new_mag_phasor - old_mag_phasor)/Z_1;
% P_loss = (abs(I_23_24))^2*real(Z_1);
% Q_loss = (abs(I_23_24))^2*imag(Z_1);
%
% Base = 100;
%
% P_loss_real = P_loss *Base;
% Q_loss_real = Q_loss *Base;
```